

# Turbulence in a coastal environment: the case of Vindeby

Rieska Mawarni Putri<sup>a</sup>, Etienne Cheynet<sup>b</sup>, Charlotte Obhrai<sup>a</sup>, and Jasna Bogunovic Jakobsen<sup>a</sup>

<sup>a</sup>Department of Mechanical and Structural Engineering and Materials Science, University of Stavanger, N-4036 Stavanger, Norway

<sup>b</sup>Bergen Offshore Wind Centre (BOW) and Geophysical Institute, University of Bergen, 5007 Bergen, Norway

**Correspondence:** Rieska Mawarni Putri (rieska.m.putri@uis.no)

**Abstract.** The one-point and two-point power spectral densities of the wind velocity fluctuations are studied using the observations from an offshore mast at Vindeby Wind Farm (Sea Mast West/SMW), for a wide range of thermal stratifications of the atmosphere. A comparison with predictions from the FINO1 platform (North Sea) is done to identify shared spectral characteristics of turbulence between different offshore sites. The sonic anemometer measurement data at 6, 18, and 45 m above mean sea level (amsl) are considered. These heights are lower than at the FINO1 platform, where the measurements were collected at heights between 40 m and 80 m. Although the sonic anemometers are, to some extent, affected by transducer-flow distortion, the spectrum of the along-wind velocity component are consistent with those from FINO1 when surface-layer scaling is used and for near-neutral and moderately diabatic conditions ( $z/L < 0.3$ , where  $L$  is the Obukhov length and  $z$  is the height above the surface). For strongly stable or unstable conditions, deviations from the empirical spectral model fitted to the data recorded on the FINO1 platform may be attributed to transducer-induced flow distortion and/or limited applicability of surface-layer scaling. The co-coherence of the along-wind component, estimated for vertical separations under near-neutral conditions matches remarkably well with the predictions from FINO1. These findings mark an important step toward more comprehensive coherence models for wind load calculation. The turbulence characteristics estimated from the present dataset are valuable to better understand the structure of turbulence in the marine atmospheric boundary layer and are relevant for load estimations of offshore wind turbines. Yet, the data set recorded at Vindeby and FINO1 covers only the lower part of the rotor of state-of-the-art offshore wind turbines. Therefore, further improvements in the characterisation of atmospheric turbulence for wind turbine design relies on measurements at heights above 100 m amsl.

*Copyright statement.* TEXT

## 1 Introduction

In the early 1990s, the first generations of offshore wind farms were commissioned to test the viability of extracting wind power in the marine atmospheric boundary layer (MABL). The first was Vindeby Wind Farm which provided electricity to around 2,200 homes during its 25 years of operation, with a total generated power of 243 GWh (Power Technology, 2020). The project was deemed successful and marked the beginning of the offshore wind sector.

Not only was Vindeby project the first offshore wind farm, but it also provided precious information on meteorological conditions in the MABL using offshore and onshore meteorological masts. The data collected has been used to study the characteristics of the mean wind speed profile under various atmospheric conditions (Barthelmie et al., 1994; Barthelmie, 1999). The masts were also instrumented with 3D sonic anemometers to study turbulence, but these data were used in a limited number of studies only (e.g. Mahrt et al., 1996, 2001).

The characteristics of the MABL differ from the overland atmospheric boundary layer (ABL) due to the larger proportion of the occurrence of non-neutral atmospheric stability conditions than on land (Barthelmie, 1999; Archer et al., 2016). Since the 2010s, several studies have indicated that diabatic wind conditions may significantly affect the fatigue life of offshore wind turbines (OWTs) components (Sathe et al., 2013; Hansen et al., 2014; Holtslag et al., 2016; Doubrawa et al., 2019; Nybø et al., 2020; Putri et al., 2020). Recent measurements from the first commercial floating wind farm (Hywind Scotland) have even shown the direct influence of the atmospheric stability on the floater motion (Jacobsen and Godvik, 2021). Diabatic conditions are more likely to affect floating wind turbines than bottom-fixed ones as the first few eigenfrequencies of large floating wind turbines are close to or below 0.20 Hz (Nielsen et al., 2006), which is the frequency range mainly affected by the thermal stratification of the atmosphere. To model properly the wind load for wind turbine designs, a better understanding of the spectral structure of turbulence in the MABL is necessary, which addresses partly the first of the three great challenges in the field of wind energy (Veers et al., 2019).

The limitations of current guidelines for offshore turbulence modelling, such as IEC 61400-1 (2005), have been highlighted in the past (Cheynet et al., 2017, 2018). Site-specific measurements advised by IEC 61400-1 (2005) are related to the mean flow and integral turbulence characteristics. However, for the spectral characteristics, appropriate scaling can be used to display universal shapes over specific frequency ranges. In this regard, the present study addresses similar challenges as discussed by Kelly (2018) but focuses on some specific aspects not covered by the spectral tensor of homogeneous turbulence (Mann, 1994). Firstly, the low-frequency fluctuations are generally underestimated by the uniform-shear model, especially under convective conditions (De Maré and Mann, 2014; Chougule et al., 2018). Secondly, the vertical coherence of turbulence is not always described accurately by the spectral tensor (Mann, 1994; Cheynet, 2019).

Using the unexplored sonic anemometer data from Vindeby database, this study looks at the characteristics of offshore turbulence in the frequency space. The objective is to quantify the similarities between these characteristics and those identified on FINO1 (Cheynet et al., 2018). Such a comparison is relevant to establishing new offshore wind turbulence models that can be used to improve the design of future multi-megawatt offshore wind turbines. Whereas the measurement data from FINO1 were obtained 40 km away from the shore, at heights between 40 m and 80 m above the mean sea level (amsl), those from the Vindeby database were collected only 3 km from the seaside and at heights between 6 m and 45 m amsl. Therefore, the two data sets offer a complementary description of wind turbulence above the sea.

The present study is organised as follow: Section 2 describes the instrumentation and the site topography. Section 3 summarises the data processing, the assumptions, and the models used to study the spectral characteristics of turbulence. Section 4 presents the methodology used to assess the data quality and selection of stationary velocity data. Section 5 first evaluates the applicability of surface-layer scaling for the anemometer records at 6 m amsl. Then, the one-point velocity spectra and co-coherence estimates

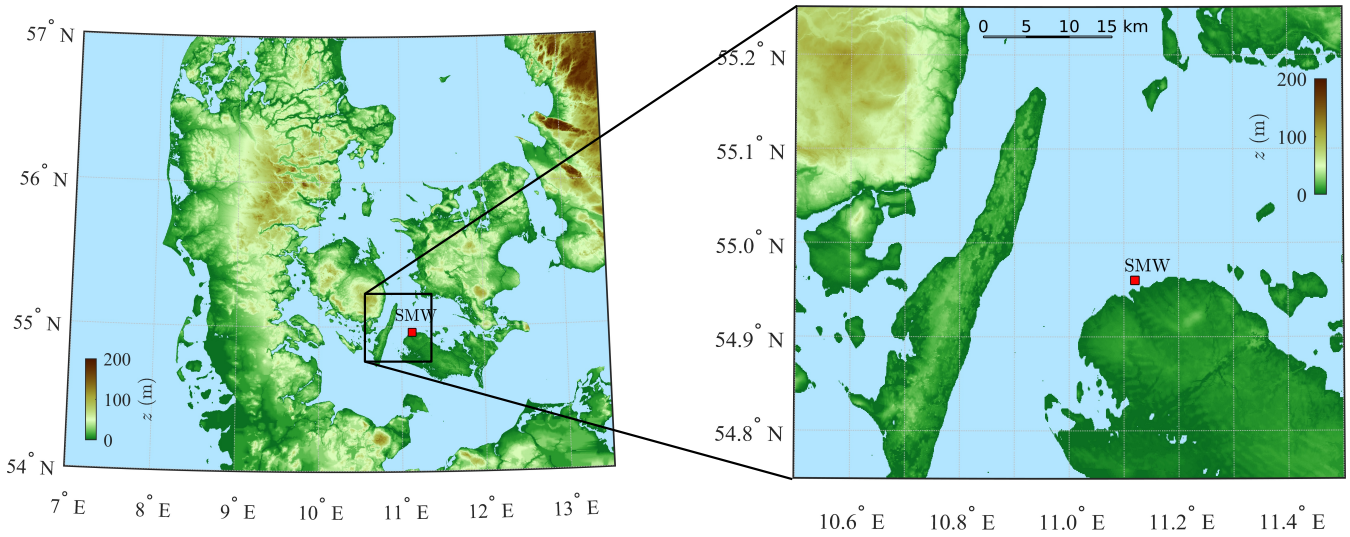


**Figure 1.** Digital elevation model of Southern Denmark showing the location of South Mast West (SMW), in a sheltered flat coastal environment.

from Vindeby are compared with predictions from semi-empirical models established on FINO1 (Cheynet et al., 2018) to assess the similarities of the spectral characteristics between the two sites. Finally, the applicability of the Vindeby database for the design of an adequate turbulence model for offshore wind turbines is discussed in Section 5.5.

## 2 Instrumentation and site description

Vindeby Wind Farm operated in Denmark from 1991 to 2016 and was decommissioned in 2017. It was located 1.5 km to 3 km from the northwestern coast of Lolland Island (fig. 1). Due to its location, Vindeby may be regarded as a coastal site instead of an offshore one. Vindeby has a flat topography with an average elevation under 11 m amsl, whereas the water depth around the wind farm ranges from 2 m to 5 m (Barthelmie et al., 1994). As pointed out by Johnson et al. (1998), the average significant wave height  $H_s$  at Vindeby is under 1 m. The water depth increases from around 3 m in the proximity of the wind farm up to approximately 20 m, away from the northern side of the wind farm.

The wind farm comprised 11 Bonus 450 kW turbines arranged in two rows with 300 m spacing along the 325°-145° line and three meteorological masts (fig. 2). The three masts were the Land Mast (LM), the Sea Mast South (SMS), and the Sea Mast West (SMW) where the two latter were placed offshore (fig. 2). Both SMS and SMW were installed in 1993 and decommissioned in 2001 and 1998, respectively. Measurements from LM and SMS were used by Barthelmie (1999) to assess the influence of the thermal stratification of the atmosphere on coastal wind climates. The present study considers only wind measurements from SMW due to the availability of the data.

SMW was a triangular lattice tower with a height of 48 m amsl as sketched in fig. 3. The booms on the SMW were mounted on both sides of the tower at 46° and 226° from the north and are referred to as the northern and southern boom, respectively.

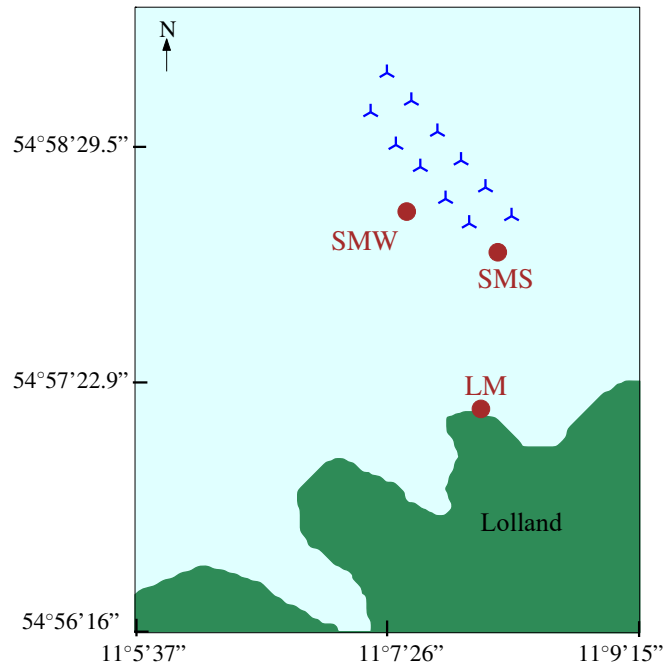


**Figure 2.** Vindeby Wind Farm layout with circles marking the position of the masts: SMW, SMS, and LM.

The booms' length ranged from 1.6 m to 4.0 m and their diameter was 50 mm (Barthelmie et al., 1994). Three F2360a GILL 3-axis ultrasonic anemometers (SAs) were mounted on the southern booms at 45, 18, and 6 m amsl and operated with a sampling rate of 20 Hz. Two Risø P2021 resolver wind vanes with wind direction transmitters P2058 were located on the northern booms at 43 m and 20 m amsl using a sampling frequency of 5 Hz. The height of the vanes' centres above the boom was 600 mm. There were seven cup anemometers mounted on SMW as shown in fig. 3. However, their measurements were not used here. The air temperature at 10 m amsl was recorded using a Risø P2039 PT 100 sensor. The sea surface elevation  $\eta$  was measured using an acoustic wave recorder (AWR) placed on the seabed, 30 m away from SMW, at a depth of 4 m (Johnson et al., 1998). The sea surface elevation data were recorded at a sampling frequency of 8 Hz but stored with a sampling frequency of 20 Hz.

The data collected from SMW were transferred to LM using an underwater fibre optic link and stored as time series of 30 min duration. Such a duration is appropriate to study turbulence at coastal and offshore areas (Dobson, 1981). Therefore, the flow characteristics studied herein are based on the averaging time of 30 min.

The fetch around SMW comprises open sea, land, and mixed fetch as shown in fig. 1. The so-called sea fetch is considered when the wind blows from 220° to 90°, with a fetch distance up to 135 km for the sector ranging from 345° to 355°. The direction sectors from 0°-50° are those most affected by flow distortion due to the presence of the mast (Barthelmie et al., 1994). Furthermore, the flow from 335°-110° might be affected by the wake effects from the wind farm. To exclude the flow disturbed by the presence of the mast and wind turbine wakes and/or internal boundary layers due to roughness changes, only the flow from 220°-330° is considered in the present study, which represents 40% of the velocity data recorded in 1994 and 1995 at SMW.

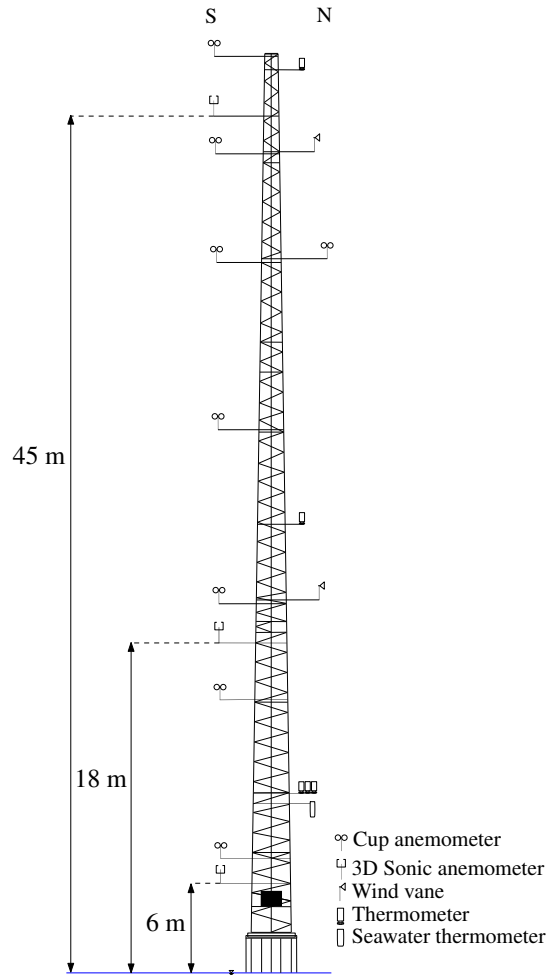


**Figure 3.** Sketch of the atmospheric instrumentation at SMW. The sonic anemometers are located in the southern boom 'S' oriented at  $226^\circ$  from the north.

The surface roughness  $z_0$  within  $247^\circ$  to  $292^\circ$  direction varies with the mean wind speed from  $1.1 \times 10^{-4}$  m to  $1.2 \times 10^{-3}$  m  
 95 (Johnson et al., 1998). A more detailed description of the other directional sectors is given by Barthelmie et al. (1994).

### 3 Theoretical background

#### 3.1 Monin-Obukhov theory

The along-wind, cross-wind, and vertical velocity components are denoted as  $u$ ,  $v$ , and  $w$ , respectively. Each component is split into a mean ( $\overline{u}$ ,  $\overline{v}$ ,  $\overline{w}$ ) and fluctuating part ( $u'$ ,  $v'$ ,  $w'$ ). In flat and homogeneous terrain, the flow is fairly horizontal, i.e.  $\overline{v}$  and  $\overline{w}$

are approximatively zero. Here, the fluctuating components are assumed to be stationary, Gaussian, ergodic random processes (Monin, 1958).

Although the  $u$ -component drives the wind turbine's rotor fatigue loads, proper modelling of the  $v$ -component in terms of power spectral density (PSD) and root-coherence may be necessary for skewed flow conditions, which can occur because of a large wind direction shear (Sanchez Gomez and Lundquist, 2020) or wind turbine yaw error (Robertson et al., 2019). To estimate a wind turbine's fatigue loads, the vertical velocity component is likely more relevant in complex terrain than offshore (Mouzakis et al., 1999). Nevertheless, this component is studied here for the sake of completeness. Also, the vertical velocity component provides precious information on the sonic anemometer flow distortion (Cheynet et al., 2019; Peña et al., 2019). The vertical velocity component is also necessary to assess the atmospheric stability using the eddy covariance method and facilitates the study of the waves' influences on the velocity data recorded by the sonic anemometers (e.g. Benilov et al., 1974).

In the atmospheric surface layer, where MOST generally applies, the scaling velocity is the friction velocity  $u_*$ , whereas the scaling lengths are the height  $z$  above the surface and the Obukhov length  $L$  (Monin and Obukhov, 1954), defined as

$$L = -\frac{u_*^3 \bar{\theta}_v}{g \kappa (\overline{w' \theta'_v})} \quad (1)$$

where  $\bar{\theta}_v$  is the mean virtual potential temperature,  $g = 9.81 \text{ ms}^{-2}$  is the gravitational acceleration,  $\kappa \approx 0.4$  is the von Kármán constant (Högström, 1985), and  $\overline{w' \theta'_v}$  is the vertical flux of virtual potential temperature. For a given height  $z$  above the surface, the non-dimensional stability parameter  $\zeta = z/L$  is used herein to classify the thermal stratification of the atmosphere.

While  $\theta'_v$  can be fairly well approximated by the fluctuating sonic temperature measurement (Schotanus et al., 1983; Sempreviva and Gryning, 1996), the mean value  $\bar{\theta}_v$  could not be reliably obtained from the sonic anemometers deployed on SMW (Kurt Hansen, private communication). Therefore,  $\bar{\theta}_v$  was obtained using the absolute temperature recorded from Risø P2039 PT 100 sensor at 10 m amsl, which was converted into the virtual potential temperature using the pressure data from LM and assuming an air relative humidity of 90% near the sea surface (Stull, 1988). The air pressure data from LM is used due to the absence of air pressure data at SMW and SMS.

Because the covariance between the cross-wind and the vertical component may not be negligible in the MABL (Geernaert, 1988; Geernaert et al., 1993), the friction velocity  $u_*$  is computed as suggested by Weber (1999), that is

$$u_* = \sqrt[4]{\overline{u'w'^2} + \overline{v'w'^2}} \quad (2)$$

A common approach to assess the applicability of MOST is to study the non-dimensional mean wind speed profile  $\phi_m$  defined as

$$\phi_m \left( \frac{z}{L} \right) = \frac{\kappa z}{u_*} \frac{\partial \bar{u}}{\partial z} \quad (3)$$

as a function of the atmospheric stability (Kaimal and Finnigan, 1994). In the following,  $\phi_m$  is empirically modelled as by Högström (1988),

$$\phi_m \approx \begin{cases} (1 + 15.2|\zeta|)^{-1/4}, & -2 \leq \zeta < 0 \\ 1 + 4.8(\zeta), & 0 \leq \zeta \leq 1 \end{cases} \quad (4)$$

The validity of eq. (4) is assessed for each anemometer in section 5.1. It should be noted that the presence of waves, especially swell, may invalidate MOST in the first few meters above the surface (Edson and Fairall, 1998; Sjöblom and Smedman, 2003b; Jiang, 2020) and this possibility will be discussed in section 5.2. Under convective conditions, the validity of MOST may also be questionable if the fetch is only a few kilometres long due to the presence of internal boundary layers (Jiang et al., 2020). In the present case, the choice of wind directions from 220° to 330° limits strongly the possibility that internal boundary layers are affecting the velocity measurements.

### 3.2 One-point turbulence spectrum

An appropriate modelling of the one-point velocity spectrum is required to compute reliably the dynamic wind-induced response and the power production of wind turbines (Sheinman and Rosen, 1992; Hansen and Butterfield, 1993). Integral turbulence characteristics, especially the turbulence intensity, are not always appropriate for turbulence characterisation (Wendell et al., 1991) which motivates the study of the spectral characteristics of turbulence herein.

Following Kaimal et al. (1972), the normalised surface-layer one-point velocity spectra express a universal behaviour in the inertial subrange

$$\frac{f S_u(f)}{u_*^2 \phi_\epsilon^{2/3}} \simeq 0.3 f_r^{-2/3} \text{ at } f_r \gg 1 \quad (5)$$

$$\frac{f S_v(f)}{u_*^2 \phi_\epsilon^{2/3}} \approx \frac{f S_w(f)}{u_*^2 \phi_\epsilon^{2/3}} \simeq 0.4 f_r^{-2/3} \text{ at } f_r \gg 1 \quad (6)$$

where  $f_r = f z / \bar{u}$  and  $f$  is the frequency;  $S_u$ ,  $S_v$ , and  $S_w$  are the velocity spectra for the along-wind, cross-wind, and vertical velocity component, respectively;  $\phi_\epsilon$  is the non-dimensional turbulent kinetic energy dissipation rate (Wyngaard and Coté, 1971):

$$\phi_\epsilon = \frac{\kappa z \epsilon}{u_*^3} \quad (7)$$

where  $\epsilon$  is the turbulent kinetic energy dissipation rate. In the present case,  $\phi_\epsilon$  is modelled as (Kaimal and Finnigan, 1994)

$$\phi_\epsilon^{2/3} = \begin{cases} 1 + 0.5|\zeta|^{2/3}, & \zeta \leq 0 \\ (1 + 5\zeta)^{2/3}, & \zeta \geq 0 \end{cases} \quad (8)$$

Equations (5) and (6) lead to the following relationships

$$\frac{S_v}{S_u} \approx \frac{S_w}{S_u} \simeq 1.33 \text{ at } f_r \gg 1 \quad (9)$$

Equation (9) is known as the assumption of local isotropy in the inertial subrange (Kolmogorov, 1941), although the latter may be reached without local isotropy (Mestayer, 1982; Chamecki and Dias, 2004). Equation (9) provides convenient relationships not only to assess the data quality (Peña et al., 2019; Cheynet et al., 2019), but also to study the influence of waves on atmospheric turbulence, since a deviation from the 4/3 law may be observed in the case of mixed-sea or swell (Smedman et al., 2003).

### 3.3 The coherence of turbulence

The coherence of turbulence describes the spatial correlation of eddies. **The root-coherence is defined as the normalised cross-spectral density of turbulence and is a complex-valued function.** The real part of the root-coherence known as the co-coherence, is one of the governing parameters for the structural design of wind turbines (IEC 61400-1, 2005). At vertical separations, the co-coherence  $\gamma_i$ , where  $i = \{u, v, w\}$ , is defined as:

$$\gamma_i(z_1, z_2, f) = \frac{\text{Re}\{S_i(z_1, z_2, f)\}}{\sqrt{S_i(z_1, f)S_i(z_2, f)}} \quad (10)$$

where  $S_i(z_1, z_2, f)$  is the two-point cross-spectral density between heights  $z_1$  and  $z_2$ , whereas  $S_i(z_1, f)$  and  $S_i(z_2, f)$  are the one-point spectra estimated at heights  $z_1$  and  $z_2$ , respectively.

Davenport (1961) proposed an empirical model to describe the co-coherence for vertical separations, which depends only on a decay parameter  $c^i$  and a reduced frequency  $n$ :

$$\gamma_i(n) \approx \exp(-c^i n) \quad (11)$$

$$n = \frac{2fd_z}{\bar{u}(z_1) + \bar{u}(z_2)} \quad (12)$$

where  $d_z = |z_1 - z_2|$ . For three heights  $z_1 > z_2 > z_3$  such that  $z_1 - z_2 = z_2 - z_3$ , Davenport's model predicts that  $\gamma_i(z_1, z_2, f)$  and  $\gamma_i(z_2, z_3, f)$  collapse onto a single curve when expressed as a function of  $n$ . This behaviour, referred to as the Davenport's similarity herein, is questioned by Bowen et al. (1983) for vertical separations and by Kristensen et al. (1981) and Sacré and Delaunay (1992) for lateral separations.

Bowen et al. (1983) modified the Davenport model by assuming that  $c^i$  was a linear function of the distance, i.e.

$$c^i = c_1^i + \frac{2c_2^i d_z}{(z_1 + z_2)} \quad (13)$$

Equation (13) reflects the blocking by the ground or the sea surface, which leads to an increase of the co-coherence with measurement height. This equation implies that the co-coherence decreases more slowly than predicted by the Davenport model if measurements are conducted far from the surface and at short separations. On the other hand, the co-coherence may decrease faster than predicted by the Davenport model if the measurements are associated with large separation distances. This implies that fitting the Davenport model to measurements with short or large separations may only lead to an inadequate design of wind turbines.

The model by Bowen et al. (1983) was further modified by Cheynet (2019) by including a third decay parameter  $c_3^i$  to account for the fact that the co-coherence cannot reach values of 1 at zero frequency unless the separation distance is zero. This led to the following three-parameter co-coherence functions, which is herein referred to as the modified Bowen model:

$$\gamma_{ii}(z_1, z_2, f) = \exp\left\{-\left[\frac{|z_2 - z_1|}{\bar{u}(z_1, z_2)}\sqrt{(c_1^i f)^2 + (c_3^i)^2}\right]\right\} \exp\left(-\frac{2c_2^i f |z_2 - z_1|^2}{(z_1 + z_2)\bar{u}(z_1, z_2)}\right) \quad (14)$$

It should be noted that both  $c_1^i$  and  $c_2^i$  are dimensionless whereas  $c_3^i$  has the dimension of the inverse of a time. Following Kristensen and Jensen (1979),  $c_3^i \propto 1/T$  where  $T$  is a time scale of turbulence. Therefore, low values of  $c_3^i$  are associated with a



co-coherence converging toward 1 at low frequencies for which the separation distance is small compared to a typical turbulence length scale. The rotor diameter of multi-megawatt OWTs commissioned after 2015 in the North Sea is slightly larger than  
190 150 m. For such structures, assuming  $c_3^i \approx 0$  may no longer be appropriate.

IEC 61400-1 (2005) recommends the use of two empirical coherence formulations. The first one was derived based on the exponential coherence proposed by Davenport (1961), which read as

$$\gamma_u(f, d_z) = \exp \left\{ -12 \left[ \sqrt{\left( \frac{f d_z}{\bar{u}_{hub}} \right)^2 + \left( 0.12 \frac{d_z}{8.1 L_c} \right)^2} \right] \right\} \quad (15)$$

where  $\bar{u}_{hub}$  is the mean wind speed at the hub height and

$$L_c = \begin{cases} 0.7z, & z \leq 60 \text{ m} \\ 42 \text{ m}, & z \geq 60 \text{ m} \end{cases} \quad (16)$$

The second coherence model was derived based on a spectral tensor of homogeneous turbulence (Mann, 1994) but is not described in detail here. Further assessments of this model can be found in Mann (e.g. 1994), Saranyasoontorn et al. (2004) or Cheynet (2019).

#### 4 Data processing

200 Sonic anemometer data monitored continuously from May 1994 to July 1995 were selected. No data were collected in July 1994 and October 1994, leading to 13 months of available records. The sonic anemometer at  $z = 18 \text{ m}$  was chosen as the reference sensor throughout the data processing. The measurements at  $z = 45 \text{ m}$  were associated with a higher measurement noise than at the other two heights. Although this noise was almost negligible at wind speed above  $10 \text{ m s}^{-1}$ , it was visible in the velocity records at low wind speeds.

205 Since the wind sensors at 6, 18, and 45 m amsl were omnidirectional sonic anemometers, they were prone to flow distortion by the transducer. This flow distortion was investigated in terms of friction velocity estimated from the asymmetric solent anemometer mounted at 10 m amsl, between May 1994 and September 1994 only, due to data availability. The corrected friction velocities for the sensors at 6, 18, and 45 m were computed using the data at 10 m, as elaborated in appendix B. When using the corrected friction velocity, no significant improvement was found for the ensemble-averaged normalised PSD estimates. It was  
210 then concluded that for the relatively narrow selected sector ( $220^\circ$ - $330^\circ$ ), the application of an ensemble averaging limits the influence of the transducer-induced flow distortion on the spectral flow characteristics. Therefore, it was decided not to apply a correction for both friction velocity and the Obukhov length to avoid over-processing the data.

Both the double rotation technique and the sectoral planar fit (PF) method (Wilczak et al., 2001) were considered to correct the tilt angles of the SAs. The choice of the algorithm relied on a comparison between the friction velocity  $u_*$  estimated using  
215 eq. (2) and the method by Klipp (2018), which does not require any tilt correction. The latter method provides an estimate  $u_{*R}$  of the friction velocity using the eigenvalues of the Reynolds stress tensor. Following this comparison, the double rotation

technique was found to provide, in the present case, slightly more reliable results than the PF algorithm (see appendix A). It should be noted that this finding is likely specific to the Vindeby data-set as the planar fit method usually provides **better estimates of the turbulent fluxes** (Wilczak et al., 2001).

220 The time series were sometimes affected by outliers. Here, the outliers were identified using a moving median window based on 5 min window length. The same outlier detection algorithm was also used for the sea surface elevation data, but with a moving window of 180 s. The local median values were then used to compute the median absolute deviation (MAD), as recommended by Leys et al. (2013). Data located more than five MAD away from the median were replaced with NaNs. The generalised extreme Studentised deviate test (Rosner, 1983) was also assessed to detect outliers but did not bring significant  
 225 improvements. When the number of NaNs in the time series was under 5%, they were replaced using a non-linear interpolation scheme based on the inpainting algorithm by D’Errico (2004) with the “spring” method. A more adequate but slower approach using autoregressive modelling (Akaike, 1969) was also applied but yielded a similar conclusion and therefore was not used. Time series containing more than 5% of NaNs were dismissed. Although other spike detection and interpolation algorithms exist in the literature (e.g. Hojstrup (1993)), the approach adopted in this study was found to provide an adequate trade-off between  
 230 computation time and accuracy.

To assess the first- and second-order stationarity of the velocity recordings, the moving mean and the moving standard deviation of the along-wind component were calculated using a window length of 10 min. The time series were considered as stationary when the two following criteria were fulfilled: (1) the maximum absolute relative difference between the moving mean and the static mean was lower than a threshold value of 20%; (2) for the moving standard deviation, the maximum absolute  
 235 relative difference was also used with a threshold value of 40%. The choice of a larger threshold value for the moving standard deviation test is justified by the larger statistical uncertainty associated with the variance of a random process compared to its mean (Lumley and Panofsky, 1964).

Velocity records with an absolute value of skewness larger than 2 or a kurtosis below 1 or above 8 are likely to display an unphysical behaviour (Vickers and Mahrt, 1997) and were subsequently dismissed. The statistical uncertainties of the records  
 240 were quantified as by Wyngaard (1973) and Stiperski and Rotach (2016):

$$a_{ii}^2 = \frac{4z}{T\bar{u}} \left[ \frac{\overline{i'^4}}{\sigma_i^4} - 1 \right] \quad (17)$$

$$a_{uw}^2 = \frac{z}{T\bar{u}} \left[ \frac{\overline{(u'w')^2}}{u_*^4} - 1 \right] \quad (18)$$

$$a_{vw}^2 = \frac{z}{T\bar{u}} \left[ \frac{\overline{(v'w')^2}}{u_*^4} - 1 \right] \quad (19)$$

where  $a_{ij}$  with  $i, j = (u, v, w)$  is the uncertainty associated with the variance and covariance estimates. Time series with a large  
 245 random error, i.e.  $a_{ii} > 0.20$  or  $a_{ij} > 0.50$ ,  $i \neq j$ , were excluded.

The records with a mean wind speed below  $5.0 \text{ ms}^{-1}$  at 18 m amsl were discarded. Assuming a logarithmic mean wind profile, a near-neutral atmosphere, and a **roughness length  $z_0 = 2 \times 10^{-4} \text{ m}$  (WMO, 1983)**, the corresponding mean wind speed at a typical offshore wind turbine hub height (90 m amsl) is  $5.7 \text{ ms}^{-1}$ . The present choice of a lower threshold mean wind speed

**Table 1.** Percentage of the records between April 1994 to July 1995 from SMW that failed the quality-data assessment.

	6 m	18 m	45 m
NaNs > 5%	5%	< 1%	22%
Unphysical kurtosis and skewness	4%	3%	< 1%
Non-stationary	9%	15%	19%
Large statistical uncertainties	2%	4%	22%

is, therefore, consistent with the cut-in wind speed of large offshore wind turbines, which is  $5.0 \text{ m s}^{-1}$  at hub height. It ensures  
250 also a consistent comparison of the spectral characteristics of turbulence with the data collected at FINO1, where the lowest  
mean wind speed considered was  $5.0 \text{ m s}^{-1}$  at 80 m amsl.

The PSD estimates of the velocity fluctuations were evaluated using Welch’s method (Welch, 1967) with a Hamming window,  
three segments, and 50% overlap. The spectra were ensemble-averaged using the median of multiple 30 min time series that  
passed the data-quality tests described above and were smoothed by using bin-averaging over logarithmically-spaced bins. The  
255 co-coherence estimates were also computed using Welch’s method but using eight segments and 50% overlap to further reduce  
the statistical uncertainty.

Table 1 displays the percentage of samples at each measurement height that failed the data-quality assessment. It relies on  
initial data availability of 86%, 97%, and 86% for the anemometers at 6, 18, and 45 m amsl, respectively. Following the criteria  
used in the data processing and Table 1, the percentage of data considered for the analysis was 69%, 76%, 45% at 6, 18, and  
260 45 m amsl, respectively. These percentages correspond to 1566 time series of 30 min duration for the SA at 6 m, 1771 time  
series at 18 m, and 854 at 45 m. The data from SA at 45 m showed the highest portion of non-stationary and large statistical  
uncertainties compared to the other SAs. Furthermore, the SA at 45 m also contained the highest fraction of NaNs in the time  
series, due to a large number of outliers. The larger fraction of data removal for the anemometer at 45 m is attributed to the  
observed uncorrelated white noises in the signal. This measurement noise, which may be linked to the length of the cable joining  
265 the anemometer and the acquisition system, is usually small for wind speed above  $10 \text{ m s}^{-1}$ . Therefore, it was decided not to  
filter it out using digital low-pass filtering techniques. Time series that were flagged as non-physical made up less than 5%  
for each SA in the present data set, likely because the test was applied after the outlier detection algorithm. The portion of  
non-stationary time series increased with height (see Table 1). Closer to the surface, the eddies are smaller and are less likely to  
be affected by the sub-meso or mesospheric atmospheric motion, which contribute to non-stationary fluctuations (Högström  
270 et al., 2002).

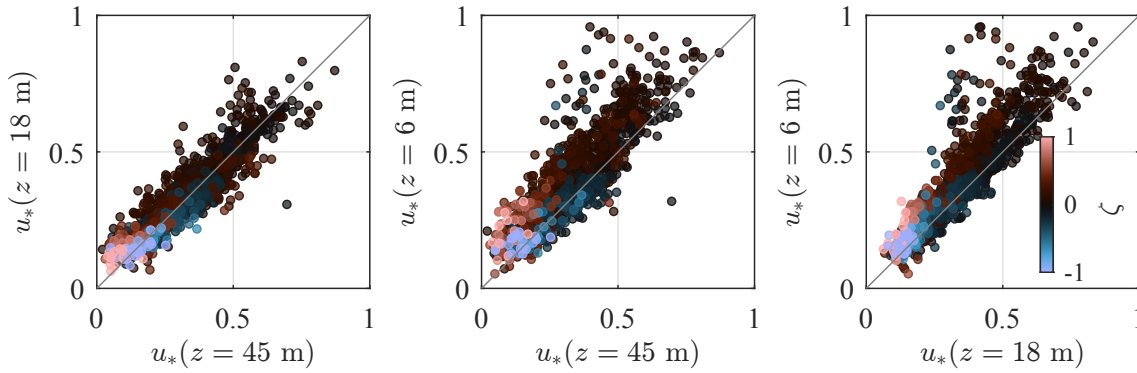


**Figure 4.** Friction velocity estimated by the three sonic anemometers on SMW for a wide range of stability conditions with  $|\zeta| < 2$ .

## 5 Results

### 5.1 Applicability of MOST

In the atmospheric surface layer, the friction velocity  $u_*$  is often assumed constant with the height (constant flux layer). However, fig. 4 shows that the friction velocity is generally larger at 6 m than at the other two measurement heights, especially under  
 275 stable conditions. The different friction velocity values at 6 m compared to 18 m and 45 m were suspected to be due to the transducer-induced flow distortion and/or the contribution of the wave-induced stress to the total turbulent stress (Janssen, 1989; Tamura et al., 2018).

The applicability of MOST is assessed by studying  $\phi_m$  as a function of  $\zeta$ . The similarity relation describing the mean wind speed profile agrees well with the sonic anemometer measurements under all stability conditions except between the sensor  
 280 at 6 m and 18 m amsl at  $\zeta > 0.3$ . It should be noted that at 6 m amsl, the local estimate of  $\zeta$  shows a much greater portion of near-neutral conditions than at 18 m amsl. The right panel of fig. 5 does not show such a deviation, maybe because the friction velocity estimated at 45 m amsl is slightly underestimated due to the high-frequency noise in the velocity records of the top sensor. This further justifies the use of the sonic anemometer at 18 m amsl to estimate the non-dimensional stability parameter  $\zeta$ .

The distribution of  $\zeta$  as a function of the mean wind speed  $\bar{u}$  is given in fig. 6 for the sector between  $220^\circ$  and  $330^\circ$ . The  
 285 majority (82%) of the stationary records samples were associated with a wind speed between  $7 \text{ ms}^{-1}$  to  $15 \text{ ms}^{-1}$  at 18 m amsl. Non-neutral conditions are defined herein as situations where  $|\zeta| > 0.1$ . They represent 69% of the samples at  $\bar{u} < 12 \text{ ms}^{-1}$  and 12% at  $\bar{u} \geq 12 \text{ ms}^{-1}$ . The distribution of the atmospheric stability conditions is in overall agreement with Barthelmie (1999) and Sathe and Bierbooms (2007) for Vindeby site.

The local isotropy is evaluated by the spectral ratios  $S_v/S_u$  and  $S_w/S_u$  for near-neutral conditions ( $-0.1 \leq \zeta \leq 0.1$ ). The  
 290 spectral ratios are presented in fig. 7. As documented by e.g. Chamecki and Dias (2004), Cheynet et al. (2018) or Peña et al. (2019), the ratio  $S_v/S_u$  reaches isotropy more easily than  $S_w/S_u$ . The presence of significant measurement noise in the velocity data at the top sensor leads to ratios  $S_v/S_u$  and  $S_w/S_u$  that reach a maximum at  $f_r \approx 3$  before decreasing at higher frequencies. The isotropic values of  $S_w/S_u$  are only reached for the sensors located at 6 m amsl. Smedman et al. (2003) observed that the

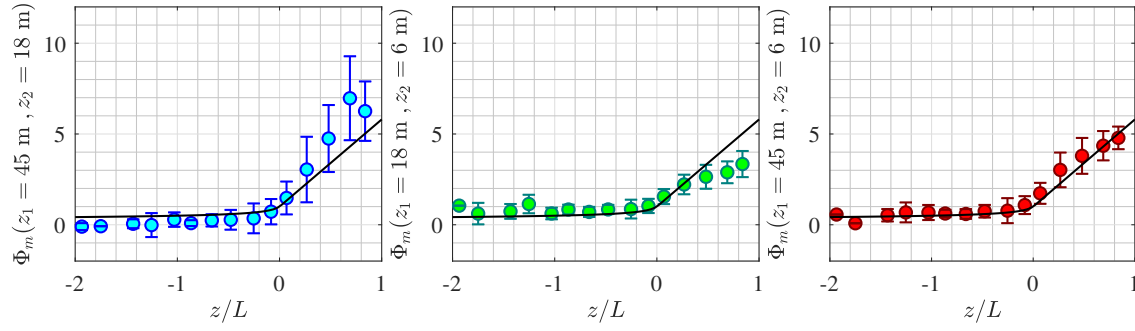


**Figure 5.** Variation of  $\phi_m$  with the non-dimensional stability parameter  $\zeta$  estimated from SA at 18 m amsl. The solid black line is eq. (4) and the error bar represents the interquartile range.

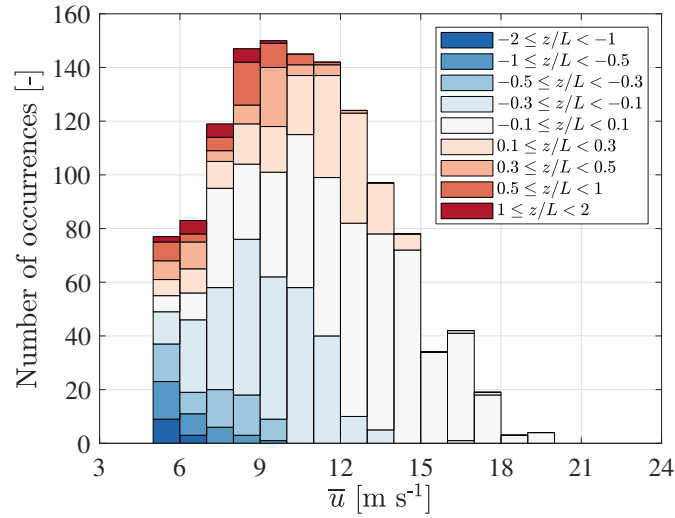


**Figure 6.** Stability distribution as a function of mean wind speed for the considered fetch (220°-330°) at height  $z = 18$  m.

maximum value of  $S_w/S_u$  is close to or below unity in the presence of a swell sea-state. Figure 7 shows that a similar deduction is not applicable here, because the wind-sea conditions are predominant. At 18 m amsl, the ratio  $S_w/S_u$  converges toward 1.2 in near-neutral conditions, i.e. slightly below the theoretical value of 1.33 (Kolmogorov, 1941). This value is similar to the ratio estimated from data measured at FINO1 (Cheynet et al., 2018) or in Peña et al. (2019) and can be attributed to flow distortion by the instrument.

## 5.2 Wind-wave interactions

The close proximity of the sensor at 6 m with the sea surface is used to study the potential influence of the wave boundary layer (WBL) (Sjöblom and Smedman, 2003a). This layer is also called the wave sublayer by Emeis and Türk (2009), who suggest that

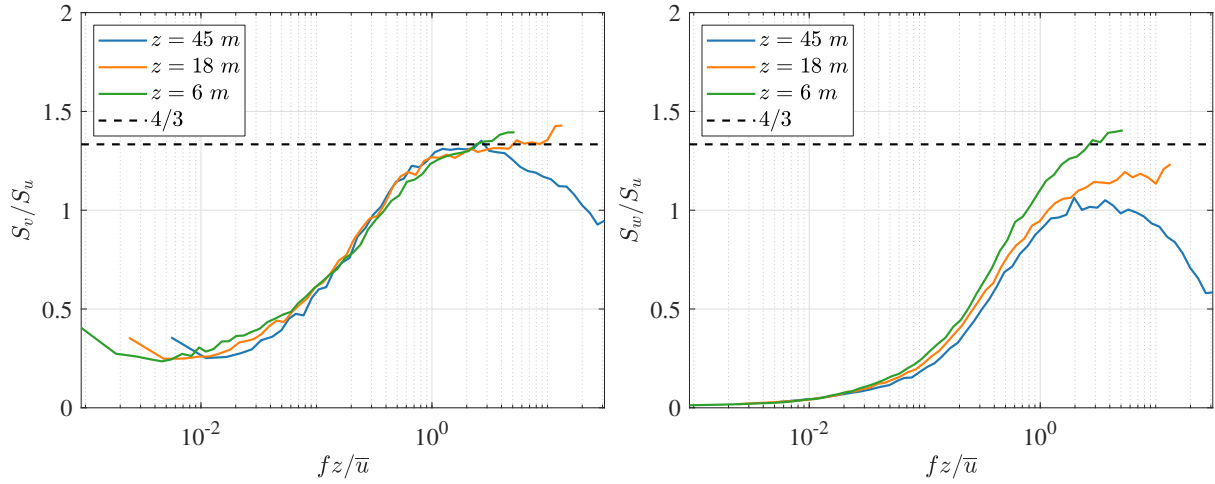


**Figure 7.** Spectral ratio  $S_v/S_u$  (left panel) and  $S_w/S_u$  (right panel) for near-neutral conditions. The dashed line represents the theoretical  $4/3$  value associated with local isotropy in the inertial subrange.

its depth is approximately  $5H_s$ , although there is no consensus on the depth of the WBL. The objective of this subsection is to identify whether the wave-induced turbulence can be detected in the velocity records at 6 m amsl due to the observed turbulence characteristics in section 5.1.

305 Here, the measurements are explored in terms of wind-wave interactions, using the wave elevation data collected by the AWR near SMW. A total of 925 high-quality samples collocated in time with the wind velocity data studied were identified. Each wave elevation record was 30 min long and corresponded to a wind direction between  $220^\circ$  and  $330^\circ$ . There exist methods to filter out the wave-induced velocity component from the turbulent velocity component (e.g. Hristov et al. (1998)), but these methods are not addressed herein for brevity.

310 The term “high-quality samples” refers to the sea surface elevation time histories  $\eta(t)$  without flattened valleys or significant measurement noises at frequencies under  $f_t = 0.10$  Hz, which were sometimes observed in the records. The identified wave peak period  $T_p$  was generally located at frequencies above 0.20 Hz, which justifies the choice of a threshold frequency of 0.10 Hz. More precisely, the contribution of wave elevation data at frequencies below  $f_t$  to the variance of the signal was negligible unless non-stationary fluctuations were recorded. The sea surface elevation skewness ranged from  $-0.02$  to  $0.37$  with a median

315 value of  $0.17$ , while the kurtosis varied from  $2.7$  to  $3.4$  and a median value of  $3$ . Therefore,  $\eta$  time series can be assumed Gaussian on average and the significant wave height  $H_s$  was approximated as  $4\sigma_\eta$  where  $\sigma_\eta$  is the standard deviation of the sea surface elevation (Longuet-Higgins, 1952). Nonetheless, it should be emphasised that these results are concluded based on the measurement at one location near SMW, and the wave characteristics upstream of the mast are unexplored.

Hourly hindcast data with a 2 km horizontal resolution (Tuomi and Huess, 2020) give larger  $H_s$  values than the measurement

320 data as shown in fig. 8. Close to the coast and in shallow water areas, the accuracy of hindcast data is usually lower, while the relatively low accuracy of the wave measurements leads to underestimated  $H_s$  values. The measured significant wave heights

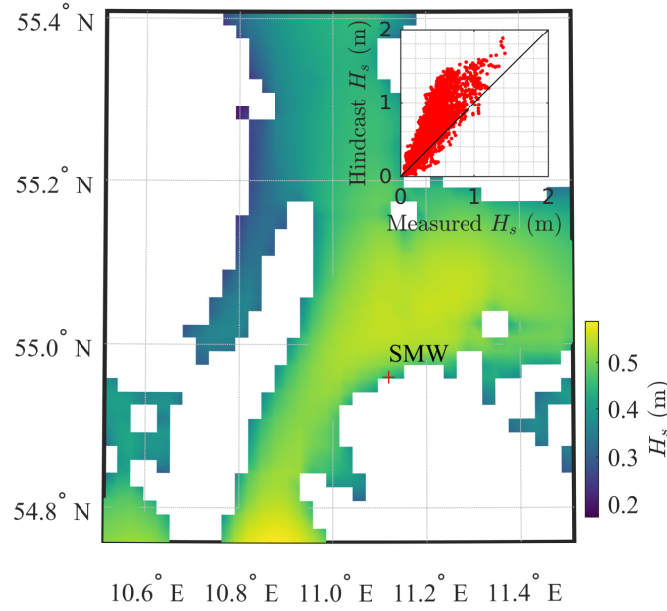


**Figure 8.** Median value of the hourly significant wave height for the year 1995 near SMW provided by the hindcast data (Tuomi and Huess, 2020). The inset compares the measured and modelled  $H_s$  values between 1994 and 1995.

were below 1.5 m during 1994 and 1995 with a median value of 0.4 m. The hindcast data provided  $H_s$  values for wind-sea, primary and secondary swell. These data indicated that wind-sea conditions were largely predominant over swell conditions, nearby SMW.

325 The interactions between wind turbulence and the sea surface were explored in terms of the co-coherence and the quad-coherence (the imaginary part of the root-coherence) between the vertical velocity component  $w$  and the velocity of the wave surface  $\dot{\eta} = d\eta/dt$ . Similar approaches were adopted earlier by e.g. Grare et al. (2013) or Kondo et al. (1972) but using the coherence and without taking advantage of the ensemble average to reduce the systematic and random error, which are typically associated with the root-coherence function. In the present case, neither the co-coherence nor the quad-coherence between  $\dot{\eta}$  and  $w$  differs significantly from zero for  $H_s < 0.7$  m. For the sensor at 6 m amsl, a non-zero root-coherence was discernible from the background noise at  $0.7 \text{ m} < H_s < 0.9 \text{ m}$ . The co-coherence and quad-coherence estimates were significantly different from zero for  $0.9 \text{ m} \geq H_s$ , as illustrated in fig. 9, where the ensemble averaging of the 60 samples was applied to reduce the random error. The inset in fig. 9 shows that the selected records are characterised by a single spectral peak  $f_p$  located at frequencies between 0.20 Hz and 0.25 Hz, which is the frequency range where the quad-coherence is substantially different from zero. The observed co-coherence and the quad-coherence at this frequency range show the 90° out-of-phase fluctuations between  $\dot{\eta}$  and  $w$ , where the latter is lagging. The co-coherence and quad-coherence estimates between  $\dot{\eta}$  and the horizontal wind component  $u$  were also investigated but were nearly zero for the three sonic anemometers on SMW.

330

335

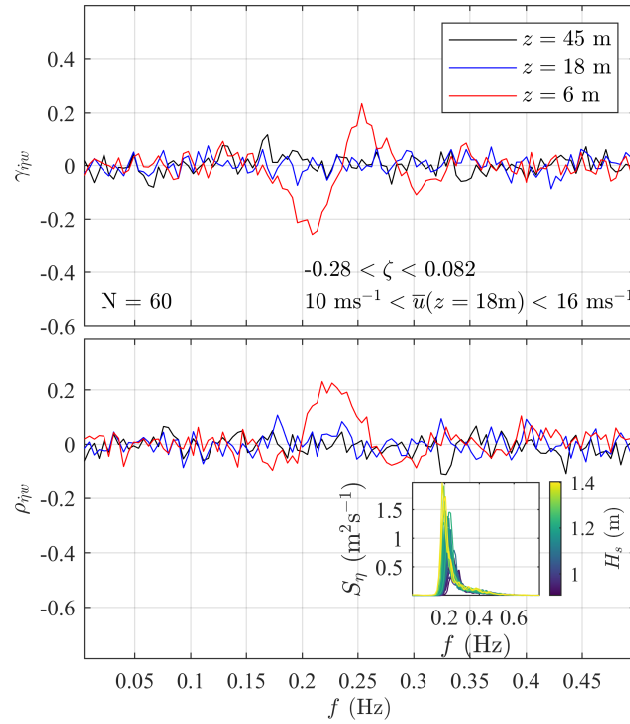


**Figure 9.** Co-coherence  $\gamma_{\dot{\eta}w}$  and quad-coherence  $\rho_{\dot{\eta}w}$  between the velocity of the wave surface  $\dot{\eta}$  and the vertical wind velocity  $w$  from the three sonic anemometers on SMW. The inset shows the individual wave elevation spectra  $S_\eta$  associated with  $H_s > 0.9$  m (60 samples) used to estimate  $\gamma_{\dot{\eta}w}$  and  $\rho_{\dot{\eta}w}$ .

The limited number of data showing a clear correlation between the velocity of the sea surface and the vertical wind component implies that the wave-induced turbulence has a limited impact on the anemometer records at 6 m. The influence of the sea surface elevation on the vertical turbulence was not clearly visible in the one-point vertical velocity spectra  $S_w$ , except for  $H_s > 1.2$  m, where a weak spectral peak near 0.2 Hz was distinguishable. The wave-induced fluctuating wind component is generally much less compared to the wind turbulence as highlighted by e.g. Weiler and Burling (1967); Kondo et al. (1972); Naito (1983). An exception may be the case of weak wind and swell conditions which are more likely to result in the observation of a sharp spectral peak near  $f_p$  in the  $S_w$  spectrum (Kondo et al., 1972). Nonetheless, as previously mentioned, such conditions are rare near SMW, most likely because SMW was located in a relatively sheltered close-water environment rather than an open ocean.

### 5.3 Turbulence spectra

When performing numerical simulations to compute the wind-induced response of wind turbines, an essential input to model the wind inflow conditions is the PSD of the velocity fluctuations. Figure 10, fig. 11, and fig. 12 depict the PSD estimates respectively for the along-wind, cross-wind, and vertical wind components as a function of the reduced frequency  $f_r$  for nine



350 stability classes. Surface-layer scaling is adopted, i.e. the PSDs are normalised with  $u_*$  (eq. (2)) and  $\phi_\epsilon^{2/3}$  (eq. (8)). Strongly non-neutral cases, defined as  $|\zeta| > 2$  are not studied herein as they are fairly uncommon for the data-set selected. The number of available samples for each stability class is denoted as  $N$  and displayed in each sub-panel.

These three figures compare the estimated spectra at  $z = 45$  m,  $z = 18$  m, and  $z = 6$  m amsl with the empirical model established on FINO1 (black solid line) at  $z = 41$  m amsl (Cheynet et al., 2018). The red curves represent the high-frequency asymptotic behaviour of surface-layer spectra for each stability class. It should be noted that the latter curves do not indicate 355 when the inertial subrange starts since the frequencies they cover were arbitrarily chosen.

In fig. 10, the maximum values of the normalised spectra for near-neutral conditions are close to unity, as described by Kaimal et al. (1972). The velocity spectra estimated at 45 m amsl show sometimes deviations from the surface-layer scaling under near-neutral and stable conditions, likely due to the observed aforementioned uncorrelated high-frequency noise, which lead to 360 an underestimation of the friction velocity. Under light and moderate unstable conditions, i.e.  $-0.3 \leq \zeta \leq -0.1$ , the velocity spectra at 6 m and 18 m amsl are similar, which supports the idea that the wave sublayer is shallower than 6 m. If  $\zeta \leq -1$ , deviations from surface-layer scaling are clearer at both 45 m and at 6 m, which is also visible in fig. 12. We remind that the non-dimensional stability parameter  $\zeta$  estimated at 6 m reflected the predominance of near-neutral conditions. This results in discrepancies between the spectral estimates at 6 m and 18 m in fig. 10 to fig. 12 which increase with  $|\zeta|$ .

365 Following surface-layer scaling, the normalised spectra at different heights should collapse onto one single curve at high frequencies, which was observed at heights between 40 m amsl and 80 m amsl at FINO1 for  $|\zeta| < 1$ . However, this is not always the case in fig. 10, fig. 11, and fig. 12. Deviations from surface-layer scaling may be partly attributed to transducer-induced flow distortion. Regarding the velocity data at 45 m amsl, the measurement noises lift the high-frequency range of the velocity spectra above the spectral slope predicted by eq. (5) or eq. (6). At 18 m amsl, eqs. (5) and (6) predict remarkably well the velocity 370 spectra at  $f_r > 3$ , indicating that surface-layer scaling is applicable at this height.

The presence of the spectral gap (Van der Hoven, 1957), separating the microscale fluctuations from the sub-meso and mesoscale ones, is noticeable at  $\zeta > 0.3$ , in line with previous observations (Smedman-Högström and Högström, 1975; Cheynet et al., 2018). Under stable conditions, the spectral gap seems to move toward lower frequencies as the height above the surface decreases. This contrasts with the observations from an onshore mast on Østerild (Denmark) by Larsén et al. (2018), which 375 indicated that the location of the spectral gap on the frequency axis was relatively constant with height.

Following Vickers and Mahrt (2003) the spectral gap timescale can be only a few minutes long under stable conditions. For  $\zeta > 0.5$ , the averaging period selected in the present study may be too large to provide reliable integral turbulence characteristics. However, filtering out the mesoscale motion may not be desirable for structural design purposes since operating wind turbines experience both turbulence and mesoscale fluctuations (Veers et al., 2019). In this regard, the use of spectral flow characteristics 380 to parametrise the wind loading on OWTs is preferable.

Under near-neutral conditions, the sensors at 6 m amsl and 18 m amsl are likely located in the so-called eddy surface layer (Högström et al., 2002; Drobinski et al., 2004), where the sea surface blocks the flow and distorts eddies. This leads to a flat spectral peak. As a result, the integral length scale would be estimated with large uncertainties. Such a spectral behaviour has

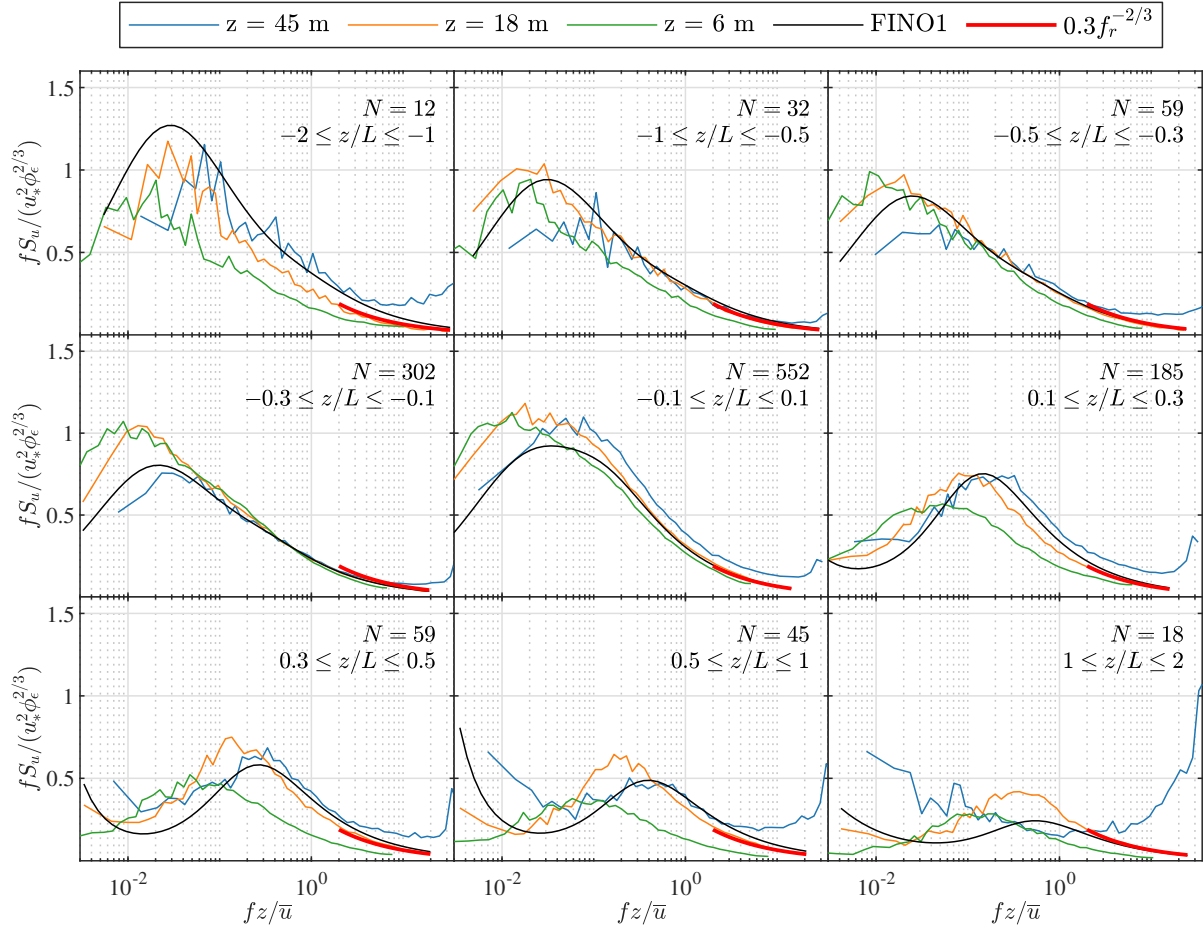


**Figure 10.** Normalised spectra of the along-wind component at 45, 18, and 6 m amsl for various stability conditions. The red curve is derived from eq. (5) and  $N$  denotes the number of samples considered for ensemble averaging.

also been observed above the eddy surface layer (Drobinski et al., 2004; Mikkelsen et al., 2017) but its consequences on wind turbine loads are unclear.

Deviations from surface-layer scaling at  $\zeta > 0.5$  may be due to the fact that the sensors are no longer located in the surface layer and/or that transducer-induced flow distortion is not negligible. For  $\zeta > 1$ , further deviations from surface-layer scaling may be related to the so-called local z-less stratification (Wyngaard and Coté, 1972) where turbulence is no longer scaled by the height above the ground.

Overall, the velocity spectra estimated at 18 m amsl and 45 m amsl at Vindeby match reasonably well with the empirical spectra estimated at 41 m amsl on FINO1 for  $-2 \leq \zeta < 1$ . This comparison is encouraging for further explorations of the surface-layer turbulence characteristics at coastal and offshore sites. Nonetheless, detailed wind measurements at heights

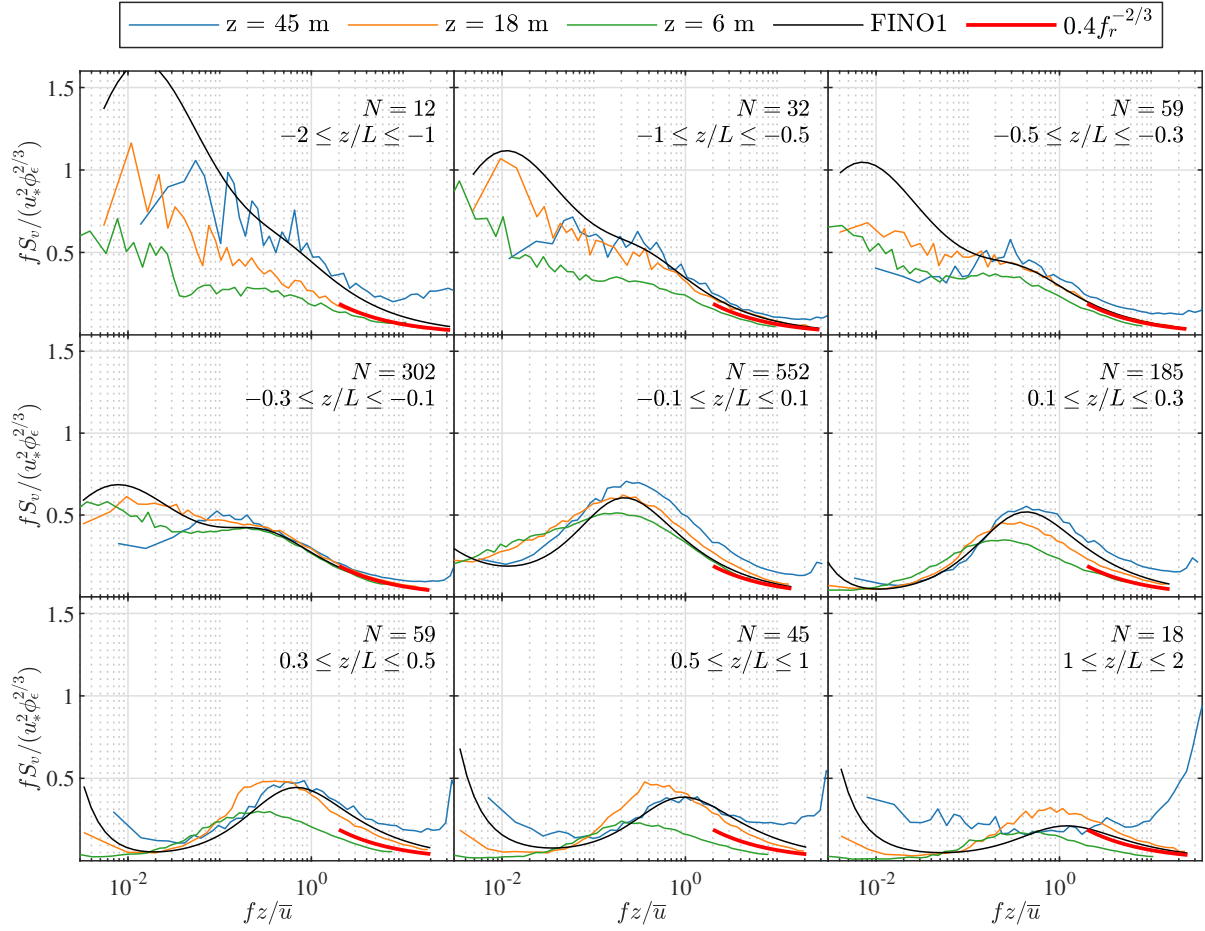


**Figure 11.** Normalised spectra of the cross-wind component at 45, 18, and 6 m amsl for various stability conditions. The red curve is derived from eq. (6) and  $N$  denotes the number of samples considered for ensemble averaging.

$z \geq 100$  m are needed to get a complete overview of the turbulence characteristics in the MABL that is relevant for OWT designs.

#### 395 5.4 Co-coherence of turbulence

The vertical co-coherence of the along-wind, cross-wind, and vertical wind components are denoted by  $\gamma_u$ ,  $\gamma_v$ , and  $\gamma_w$ , respectively. Under near-neutral conditions ( $|\zeta| \leq 0.1$ ), these are expressed as a function of  $kd_z$  in fig. 13 where  $k = 2\pi f/\bar{u}$  is the wave number, assuming that turbulence is frozen (Taylor, 1938). The co-coherence estimates are presented for three separation distances  $d_z$  because three measurement heights ( $z_1 = 45$  m,  $z_2 = 18$  m, and  $z_3 = 6$  m) were used. The co-coherence  
 400 estimated on SMW are compared to the IEC coherence model (eq. (15)) and the modified Bowen model (eq. (14)). For the latter

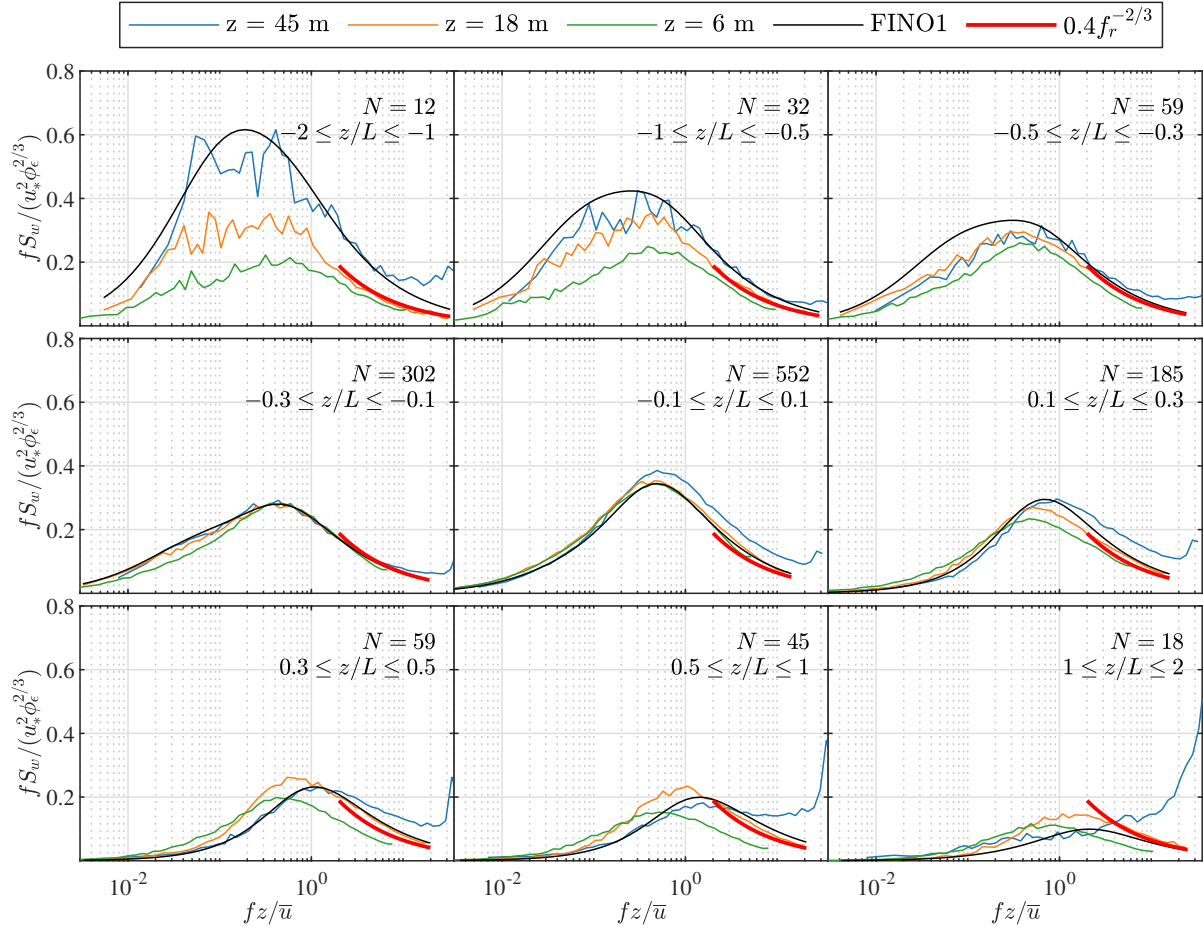


**Figure 12.** Normalised spectra of the vertical wind component at 45, 18, and 6 m amsl for various stability conditions. The red curve is derived from eq. (6) and  $N$  denotes the number of samples considered for ensemble averaging.

model, the parameters estimated on FINO1 (Cheynet, 2019) are directly used. The decay coefficients used for eq. (14) were, therefore,  $[c_1^u, c_2^u, c_3^u] = [6.0, 17.8, 0.02]$  and  $[c_1^w, c_2^w, c_3^w] = [2.7, 4.0, 0.16]$  as well as  $[c_1^v, c_2^v, c_3^v] = [0, 23.0, 0.09]$ .

Figure 13 shows that the coefficients of the modified Bowen model estimated on FINO1 apply very well to  $\gamma_u$  estimated on SMW. Larger deviations are observed for the cross-wind components, for which  $\gamma_v$  displays large negative values, especially for separations between 6 m amsl and 45 m amsl. On FINO1, the negative part of  $\gamma_v$  was relatively small, which justified the use of eq. (14) with no negative co-coherence values. Following Bowen et al. (1983); ESDU 85020 (2002) or Chougule et al. (2012), the negative part is a consequence of the phase difference and is non-negligible for the cross-wind component, which is also observed in the present case. Since this phase difference increases with the mean wind shear, it is more visible at SMW than at FINO1, where the measurements are at greater heights than at SMW.

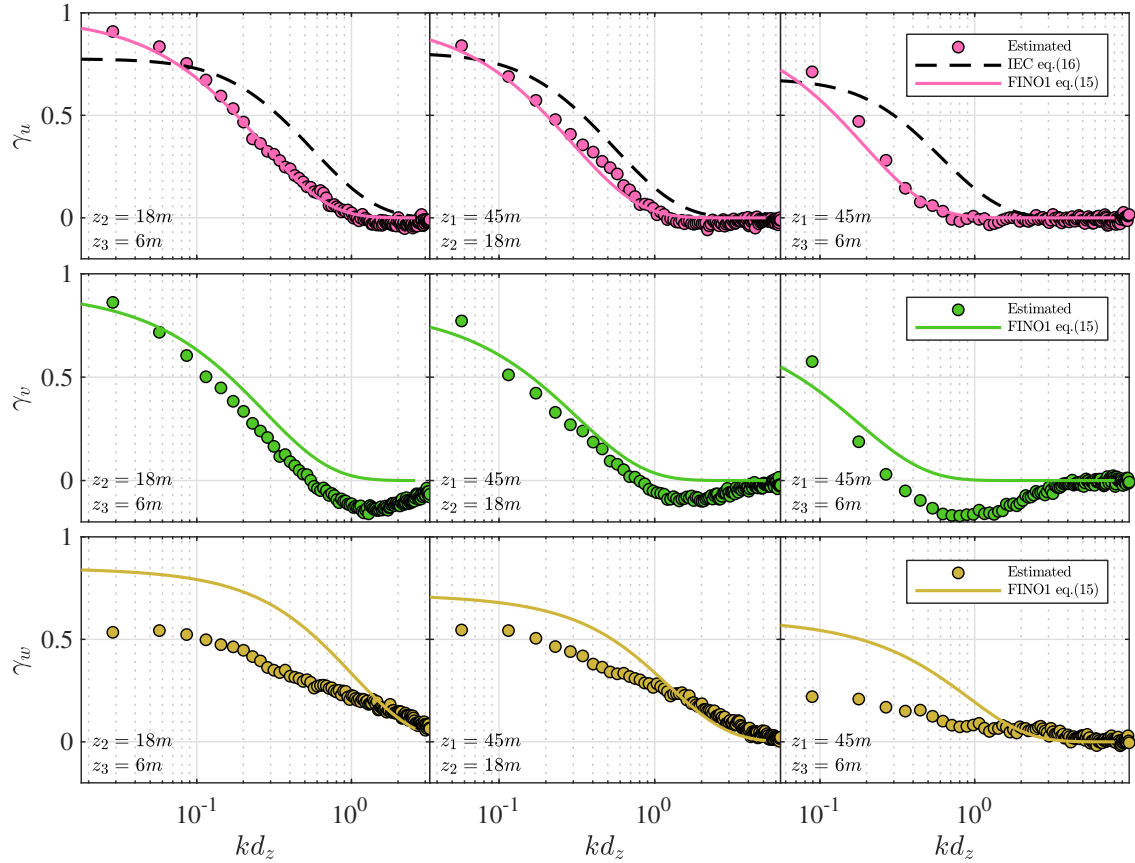


**Figure 13.** Co-coherences of the along-wind (top panels), lateral (middle panels), and vertical velocity components (lower panels) for  $|\zeta| \leq 0.1$  at three different vertical separation distances. The dots represent the measurement and the lines mark the predictions using the IEC exponential coherence model (dashed line) and the Modified Bowen model (solid line) with the fitted coefficients from FINO1 (Cheynet, 2019).

410 The IEC exponential coherence model over-predicts  $\gamma_u$  when the measurement height decreases and when the separation distance increases because this model follows fairly well Davenport's similarity, except at  $kd_z < 0.1$ . In Cheynet (2019), the Davenport model was suspected to lead to an overestimation of the turbulent wind loading on OWTs. The present results indicate that a similar overestimation may be obtained if the IEC exponential coherence model is used. Further studies are, however, needed to better quantify this possible overestimation in terms of dynamic wind loading on the wind turbine's rotor and tower, as well as on the floater's motions in the case of a floating wind turbine. Finally, additional data collection is needed to study the co-coherence at lateral separations, which is required for wind turbine design since it was not available at FINO1 nor SMW.

415

Figure 14 shows a clear variation of the estimated co-coherence with thermal stratification of the atmosphere for the three turbulence components. As observed by e.g. Soucy et al. (1982) or Cheynet et al. (2018) and modelled by Chougule et al. (2018), the vertical co-coherence is generally highest for convective conditions and smallest for stable conditions. Such results

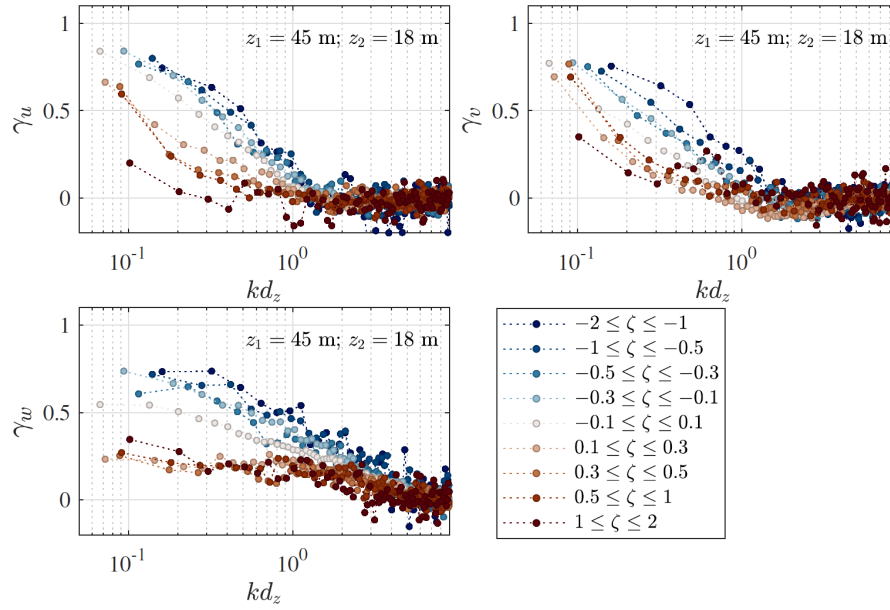


**Figure 14.** Co-coherence of the along-wind (top left), cross-wind (top right) and vertical (bottom-left) velocity components for nine stability classes, given by  $\zeta 0z/L$ . The separation distance is 27 m, between the sensors at 18 m and 45 m amsl.

reinforce the idea that modelling the turbulent loading on offshore wind turbines using a coherence model established for neutral conditions may only be appropriate for the ultimate limit state design but not for the fatigue life design.

### 5.5 Relevancy of the database for load calculation of OWTs

This study provides a thorough overview of the MABL spectral turbulence characteristics with respect to the variation of the atmospheric stability at SMW. However, its direct applicability for the designs of OWTs should be assessed carefully due to the assumptions made in the data analysis.

The presented results do not include the non-stationary conditions encountered in the field, which were removed before the analysis. About 20% of the data were disregarded as non-stationary to establish reliable spectra and co-coherence estimates. In the present case, non-stationary fluctuations were mainly associated with frequencies close to or below 0.05 Hz. For typical spar-type and semisubmersible OWT floaters, these frequencies encompass the quasi-static motions and few lowest eigen-frequencies of the floaters (Jonkman and Musial, 2010; Robertson et al., 2014). Additionally, the non-stationary turbulence fluctuations could result in non-Gaussian loadings, which could further lead to underestimation of fatigue loading (Benasciutti and Tovo, 2006, 2007).

Furthermore, the present data-set was recorded at heights lower than the hub height of the recent and the future OWTs, which is around 130 m (e.g. GE Renewable Energy, 2021). At such heights, MOST may no longer be applicable (Peña and Grynning,

2008; Cheynet et al., 2021). Above the surface layer, the velocity spectra may become independent of the height above the surface, which is coarsely accounted for in IEC 61400-1 (2005).

## 6 Conclusions

This study explores the turbulence spectral characteristics from wind records of a year duration on an offshore mast called South Mast West (SMW) near the first offshore wind farm Vindeby. We aim to identify similarities between the turbulence characteristics estimated on the FINO1 platform in the North Sea and those at Vindeby. Such an investigation is crucial to establish appropriate turbulence models relevant for the design of offshore wind turbines (OWTs). The data-set analysed was acquired by 3D sonic anemometers at 6, 18, and 45 m above mean sea level (amsl), which complements the data-set collected between 40 m and 80 m amsl on FINO1 (Cheynet et al., 2018).

The correlation between the sea surface elevation and the vertical turbulent fluctuations at 6 m amsl is quantified in terms of co-coherence between the vertical turbulent component and the velocity of the sea surface elevation. However, it is clearly visible for significant wave heights  $H_s$  exceeding 0.9 m only. Therefore, it is concluded that the sonic anemometers are located above the wave boundary layer most of the time.

The measurements at 18 m amsl follow fairly well surface-layer scaling, as expected. Because the sensors at 6 m and 18 m are located in the lower part of the surface layer, a wide spectral peak for near-neutral stratification is observed, which reflects the distortion of the eddies as they scrape along the surface. For  $\zeta = |z/L| \leq 0.3$ , the power spectral density of the along-wind velocity component at 18 m and 45 m are consistent with the empirically-defined spectral models estimated at 41 m on FINO1 (Cheynet et al., 2018). In the present case, most of the wind records are associated with  $|\zeta| < 0.3$ . Nonetheless, for  $|\zeta| > 0.3$ , deviations from the empirical spectral model fitted to the data recorded on the FINO1 platform may be attributed to transducer-induced flow distortion and/or limited applicability of the surface-layer scaling.

The co-coherence estimates of the along-wind component for neutral atmospheres are well-described by the same 3-parameter exponential decay function as used at FINO1 (Cheynet, 2019). However, this is not the case for the lateral wind components due to the closer distance to the sea surface which amplifies the phase differences between measurements at two different heights. For the vertical component, the co-coherence decreases faster than the predicted values at FINO1 (Cheynet et al., 2018). Under stable stratification, the co-coherence estimates of the three turbulent components ( $\gamma_u$ ,  $\gamma_v$ , and  $\gamma_w$ ) are significantly lower than for near-neutral conditions, in particular for  $kd_z < 1$ . On the other hand,  $\gamma_u$ ,  $\gamma_v$ , and  $\gamma_w$  are slightly higher for convective conditions compared to near-neutral conditions at  $kd_z < 1$ . Since the co-coherence is one of the governing parameters for wind loading on structures, its dependency on the atmospheric stability, which is rarely documented in the marine atmospheric boundary layer may become essential to establish design criteria for OWT fatigue life. The variability of Hywind Scotland wind turbines' floater motion with atmospheric stability (Jacobsen and Godvik, 2021) may be one example that demonstrates the importance of stability-corrected co-coherence on OWT responses.

The comparison between the turbulence characteristics at Vindeby and FINO1 is valuable to further develop comprehensive spectral turbulence models that are suitable for modern OWT designs. Nevertheless, wind loading calculations require the



knowledge of turbulence characteristics at heights up to 250 m, which is not possible at SMW or FINO1. Therefore, it is necessary for future atmospheric measurements to cover this height, where the surface-layer scaling may no longer be applicable.

470 *Code availability.* TEXT

*Data availability.* TEXT

*Sample availability.* TEXT

*Video supplement.* TEXT

**Appendix A: Sonic anemometer tilt correction**

475 The friction velocity estimates using the double rotation technique, sectoral planar fit and the method by Klipp (2018) are compared in fig. A1. In general, the friction velocity estimates from both methods are in good agreement. The average correlation coefficient for all heights is 0.985 for  $|\zeta| \leq 2$ . The PF algorithm leads to a slightly larger scatter between  $u_{*R}$  and  $u_*$ , where the average correlation coefficient from all heights is 0.976 for  $|\zeta| \leq 2$  (Table A1). The double rotation algorithm seems to give a smaller deviation between  $u_{*R}$  and  $u_*$  than the PF algorithm in the present study, which justified the adoption of the double  
480 rotation as tilt correction method herein.

Klipp (2018) noted that  $u_{*R}$  is appropriate to estimate the friction velocity if the thermal stratification of the atmosphere is neutral only. Yet, fig. A1 suggests that Klipp’s method is performing well for non-neutral conditions too, as highlighted by the correlation coefficients in Table A1, which vary between 0.963 to 0.989. Additional studies using measurements from other coastal or offshore sites are needed to assess if such observations are recurring.

**Table A1.** Correlation coefficients between  $u_{*R}$  and  $u_*$  using the planar fit (PF) or double rotation (DR)

	$ z/L  \leq 0.1$			$0.1 <  z/L  \leq 2.0$		
	6 m	18 m	45 m	6 m	18 m	45 m
PF	0.989	0.976	0.962	0.981	0.954	0.942
DR	0.995	0.986	0.973	0.989	0.968	0.963



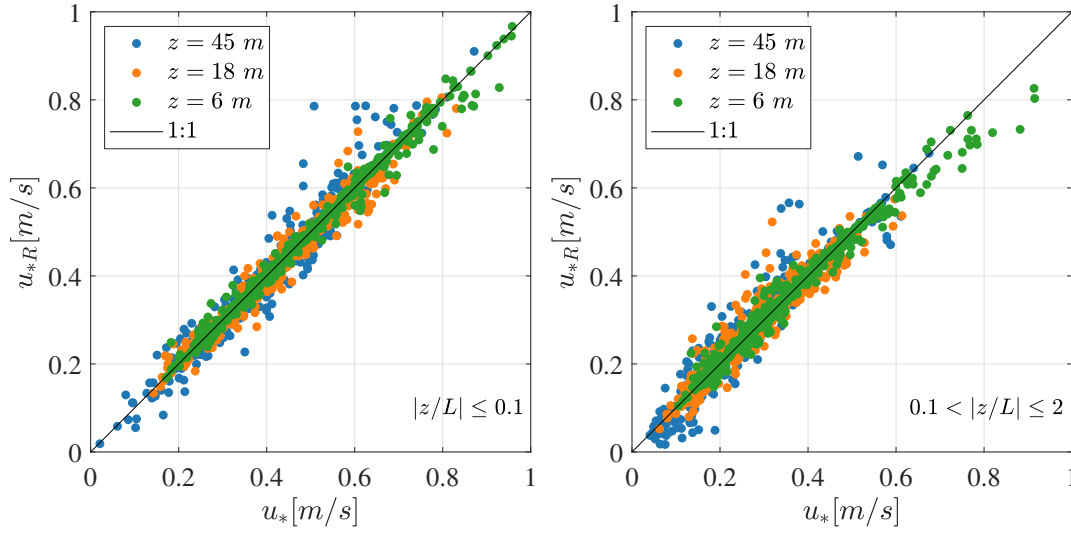


**Figure A1.** Friction velocity computed using the eddy covariance method with the double rotation method compared with the Klipp method. The left panel considers only  $|z/L| \leq 0.1$  and the right panel considers  $0.1 < |z/L| \leq 2$ .

485 The angle between the stress vector and the wind vector is given as  $\alpha = \arctan(\overline{v'w'}/\overline{u'w'})$  (Grachev et al., 2003). It is found that  $\alpha$  increases from  $8^\circ$  at 6 m amsl to  $13^\circ$  at 45 m amsl when  $\overline{v'w'} < 0$ . When  $\overline{v'w'} > 0$ ,  $\alpha$  is almost constant with the height with an average value of  $-7^\circ$ . The relatively low value of  $\alpha$ , therefore, suggests that the direction of the wind-wave-induced stress is fairly well aligned with the mean wind direction near SMW.

## Appendix B: Transducer-shadow effect

490 The sonic anemometers mounted at 6, 18, and 45 m amsl were omnidirectional solent anemometers, which can be prone to flow distortion by the transducer. Between May 1994 and September 1994, a Gill solent anemometer with an asymmetric head was installed at 10 m amsl on the southern boom of SMW (i.e. on the same side as the other three anemometers). The asymmetric head reduces the flow distortion by the transducer, at least for a specific wind sector. Although the flow distortion by the asymmetric solent was actually unknown, this sensor was used to assess the error on the friction velocity calculated with the omnidirectional solent anemometers. Only wind directions from  $220^\circ$  to  $330^\circ$  were selected, as they corresponded to the sector investigated in the present study.

Flow distortion is assumed to be a function of the angle of attack  $\alpha(z)$  and wind direction  $\theta(z)$  only. Therefore, using a multivariate regression analysis, it is possible to quantify the variability of  $u_*(z)$  with its value at 10 m, denoted  $(u_*)_{10}$  as a function of  $\alpha(z)$  and  $\theta(z)$ . For the relatively narrow sector selected, it was found that cubic functions of  $\alpha(z)$  and  $\theta(z)$  were sufficient to describe this variability. This leads to the following relationship between the friction velocity at 10 m and the one

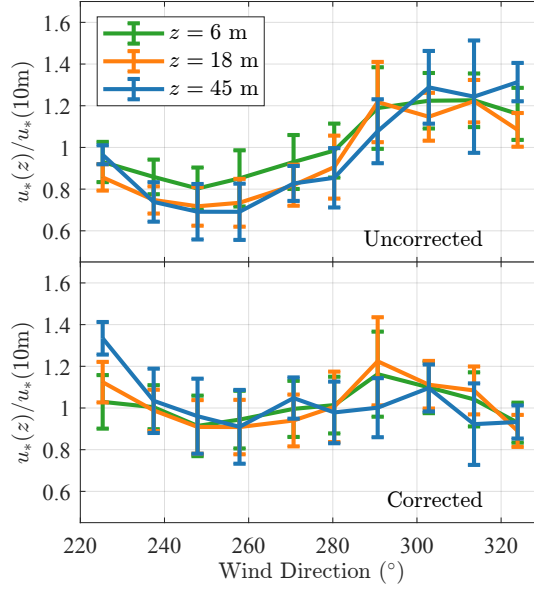


**Figure B1.** Ratio of the friction velocity by the omnidirectional solent anemometers over the one estimated at 10 m (asymmetric solent anemometer) before (top panel) and after (bottom panel) correction using a multivariate regression analysis. Velocity data recorded between May 1994 and September 1994 for the sector 220°-330° were used (480 samples of 30 min duration) and  $|z/L| < 2$  at 10 m amsl.

$u_*$  at a height  $z$ :

$$u_*(z) = (u_*)_{10} \cdot \mathbf{A} \mathbf{X}^\top \quad (\text{B1})$$

$$\mathbf{A} = \begin{bmatrix} a_1 & a_2 & a_3 & a_4 & a_5 & a_6 \end{bmatrix} \quad (\text{B2})$$

$$\mathbf{X} = \begin{bmatrix} \theta(z) & \theta(z)^2 & \theta(z)^3 & \alpha(z) & \alpha(z)^2 & \alpha(z)^3 \end{bmatrix} \quad (\text{B3})$$

where  $\mathbf{A}$  is the matrix of coefficients to be determined with the regression analysis. In eq. (B1)-eq. (B3), the friction velocity is not forced to be constant with the height and we do not assume that the flow distortion is similar for the three omnidirectional anemometers.

In the top panel of fig. B1, the maximum variations of the friction velocity between the sonic anemometer at 10 m and 18 m are  $\pm 20\%$ . When all the samples in the sector 220°-330° are averaged, the relative difference at 6, 18, and 45 m with respect to the data at 10 m are 4%, 12% and 11%, respectively. After the multivariate regression, the sector-averaged error is nearly zero, although it is clearly not zero for a given wind direction. On average, the friction velocity estimates at 6 m and 10 m are, therefore, almost identical, given that the random error on the friction velocity is above 10% for a sample duration of 30 min (Kaimal and Finnigan, 1994). As shown in fig. B1, the use of sector-averaged flow characteristics may mitigate the influence of transducer-induced flow distortion of the spectral flow characteristics estimated at 6, 18, and 45 m.

A comparison of the power spectral densities of the  $u$ -component was conducted with and without the corrected friction velocity. Only data between May 1994 and September 1994 were selected and the Obukhov length was computed at 10 m amsl.

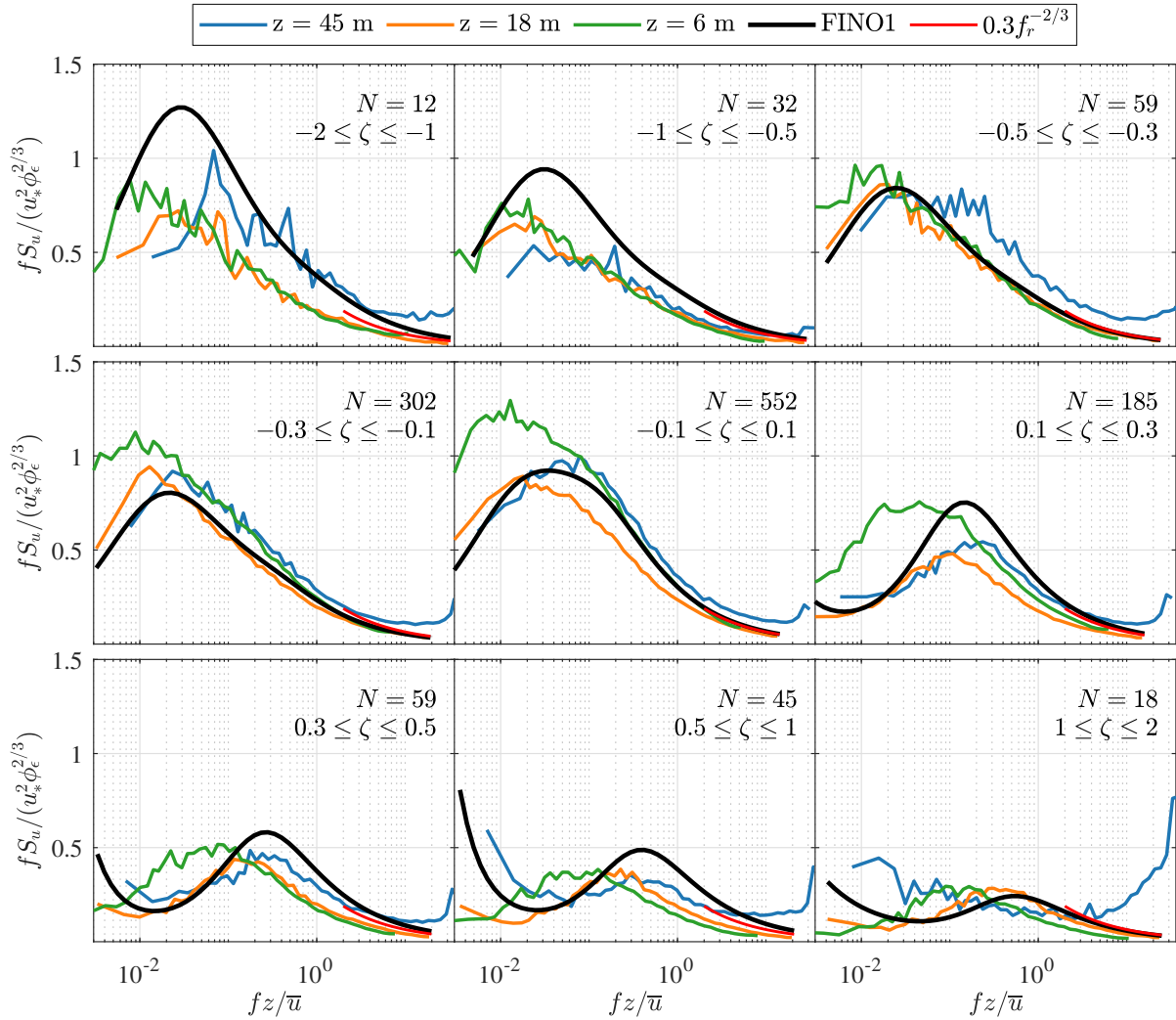


**Figure B2.** Ratio of the friction velocity by the omnidirectional solent anemometers over the one estimated at 10 m (asymmetric solent anemometer) before (top panel) and after (bottom panel) correction using a multivariate regression analysis. Velocity data recorded between May 1994 and September 1994 for the sector 220°-330° were used (480 samples of 30 min duration) and  $|z/L| < 2$  at 10 m amsl.

Five stability bins were identified in this data set. However, limited improvement was observed after the application of the correction algorithm. A further comparison was also conducted for the entire dataset, i.e. between May 1994 and July 1995 as shown in fig. B2. This resulted in similar conclusions, where the uncorrected (fig. 10) and the corrected PSDs of the  $u$ -component are not too far off. Therefore, it was decided not to use any correction for the friction velocity to avoid over-processing the data.

*Author contributions.* RMP and EC provided the data curation, formal analysis, methodology, software, and visualization. RMP and EC prepared the original draft. JBJ and CO provided the supervision, review, and editing of the manuscript. All authors contributed to the conceptualization and finalization of the paper.

*Competing interests.* The authors declare that there is no conflict of interest present.

525 *Disclaimer.* TEXT

*Acknowledgements.* The authors would like to express their gratitude to Dr Kurt Hansen for providing the Vindeby data set. Professor Joachim Reuder and Dr Stephan Kral are acknowledged for the fruitful discussion on the wave and wind conditions near SMW.

## References

- Akaike, H.: Fitting autoregressive models for prediction, *Annals of the institute of Statistical Mathematics*, 21, 243–247, 1969.
- 530 Archer, C. L., Colle, B. A., Veron, D. L., Veron, F., and Sienkiewicz, M. J.: On the predominance of unstable atmospheric conditions in the marine boundary layer offshore of the US northeastern coast, *Journal of Geophysical Research: Atmospheres*, 121, 8869–8885, 2016.
- Barthelmie, R. J.: The effects of atmospheric stability on coastal wind climates, *Meteorological Applications: A journal of forecasting, practical applications, training techniques and modelling*, 6, 39–47, 1999.
- Barthelmie, R. J., Courtney, M., Højstrup, J., and Sanderhoff, P.: The Vindeby project: A description, Tech. Rep. 741(EN), Risø National  
535 Laboratory, denmark, 1994.
- Benasciutti, D. and Tovo, R.: Fatigue life assessment in non-Gaussian random loadings, *International journal of fatigue*, 28, 733–746, 2006.
- Benasciutti, D. and Tovo, R.: Frequency-based fatigue analysis of non-stationary switching random loads, *Fatigue & Fracture of Engineering Materials & Structures*, 30, 1016–1029, 2007.
- Benilov, A. Y., Kouznetsov, O., and Panin, G.: On the analysis of wind wave-induced disturbances in the atmospheric turbulent surface layer,  
540 *Boundary-Layer Meteorology*, 6, 269–285, 1974.
- Bowen, A. J., Flay, R. G. J., and Panofsky, H. A.: Vertical coherence and phase delay between wind components in strong winds below 20 m, *Boundary-Layer Meteorology*, 26, 313–324, 1983.
- Chamecki, M. and Dias, N. L.: The local isotropy hypothesis and the turbulent kinetic energy dissipation rate in the atmospheric surface layer, *Quarterly Journal of the Royal Meteorological Society: A journal of the atmospheric sciences, applied meteorology and physical  
545 oceanography*, 130, 2733–2752, 2004.
- Cheyne, E.: Influence of the measurement height on the vertical coherence of natural wind, in: *Conference of the Italian Association for Wind Engineering*, pp. 207–221, 2019.
- Cheyne, E., Jakobsen, J. B., and Obhrai, C.: Spectral characteristics of surface-layer turbulence in the North Sea, *Energy Procedia*, 137, 414–427, 2017.
- 550 Cheyne, E., Jakobsen, J., and Reuder, J.: Velocity Spectra and Coherence Estimates in the Marine Atmospheric Boundary Layer, *Boundary-Layer Meteorology*, 169, 429–460, 2018.
- Cheyne, E., Jakobsen, J. B., and Snæbjörnsson, J.: Flow distortion recorded by sonic anemometers on a long-span bridge: Towards a better modelling of the dynamic wind load in full-scale, *Journal of Sound and Vibration*, 450, 214–230, 2019.
- Cheyne, E., Flügge, M., Reuder, J., Jakobsen, J. B., Heggelund, Y., Svandal, B., Saavedra Garfias, P., Obhrai, C., Daniotti, N., Berge, J.,  
555 Duscha, C., Wildmann, N., Husøy Onarheim, I., and Godvik, M.: The COTUR project: Remote sensing of offshore turbulence for wind energy application, *Atmospheric Measurement Techniques Discussions*, 2021, 1–32, <https://doi.org/10.5194/amt-2020-511>, 2021.
- Chougule, A., Mann, J., Kelly, M., Sun, J., Lenschow, D., and Patton, E.: Vertical cross-spectral phases in neutral atmospheric flow, *Journal of Turbulence*, p. N36, 2012.
- Chougule, A., Mann, J., Kelly, M., and Larsen, G.: *Simplification and Validation of a Spectral-Tensor Model for Turbulence Including  
560 Atmospheric Stability*, *Boundary-Layer Meteorology*, 167, 371–397, 2018.
- Davenport, A. G.: The spectrum of horizontal gustiness near the ground in high winds, *Quarterly Journal of the Royal Meteorological Society*, 87, 194–211, 1961.
- De Maré, M. and Mann, J.: Validation of the Mann spectral tensor for offshore wind conditions at different atmospheric stabilities, in: *Journal of Physics: Conference Series*, vol. 524, p. 012106, IOP Publishing, 2014.

- 565 D'Errico, J.: inpaint\_nans (<http://kr.mathworks.com/matlabcentral/fileexchange/4551-inpaint-nans>), MATLAB Central File Exchange, Retrieved, November, 2021, 2004.
- Dobson, F. W.: Review of reference height for and averaging time of surface wind measurements at sea, World Meteorological Organization, 1981.
- Doubrawa, P., Churchfield, M. J., Godvik, M., and Srinivas, S.: Load response of a floating wind turbine to turbulent atmospheric flow, Applied  
570 Energy, 242, 1588–1599, 2019.
- Drobinski, P., Carlotti, P., Newsom, R. K., Banta, R. M., Foster, R. C., and Redelsperger, J. L.: The structure of the near-neutral atmospheric surface layer, Journal of the atmospheric sciences, 61, 699–714, 2004.
- Edson, J. and Fairall, C.: Similarity relationships in the marine atmospheric surface layer for terms in the TKE and scalar variance budgets, Journal of the atmospheric sciences, 55, 2311–2328, 1998.
- 575 Emeis, S. and Türk, M.: Wind-driven wave heights in the German Bight, Ocean Dynamics, 59, 463–475, 2009.
- ESDU 85020: ESDU 85020 Characteristics of atmospheric turbulence near the ground. Part II: single point data for strong winds (neutral atmosphere), 2002.
- GE Renewable Energy: Haliade-X offshore wind turbine, <https://www.ge.com/renewableenergy/wind-energy/offshore-wind/haliade-x-offshore-turbine>, [Online; accessed 08-April-2021], 2021.
- 580 Geernaert, G.: Measurements of the angle between the wind vector and wind stress vector in the surface layer over the North Sea, Journal of Geophysical Research: Oceans, 93, 8215–8220, 1988.
- Geernaert, G., Hansen, F., Courtney, M., and Herbers, T.: Directional attributes of the ocean surface wind stress vector, Journal of Geophysical Research: Oceans, 98, 16 571–16 582, 1993.
- Grachev, A., Fairall, C., Hare, J., Edson, J., and Miller, S.: Wind stress vector over ocean waves, Journal of Physical Oceanography, 33,  
585 2408–2429, 2003.
- Grare, L., Lenain, L., and Melville, W. K.: Wave-coherent airflow and critical layers over ocean waves, Journal of Physical Oceanography, 43, 2156–2172, 2013.
- Hansen, A. and Butterfield, C.: Aerodynamics of horizontal-axis wind turbines, Annual Review of Fluid Mechanics, 25, 115–149, 1993.
- Hansen, K. S., Larsen, G. C., and Ott, S.: Dependence of offshore wind turbine fatigue loads on atmospheric stratification, Journal of Physics: Conference Series, 524, 012 165, 2014.
- 590 Högström, U.: Von Karman's constant in atmospheric boundary layer flow: Reevaluated, Journal of atmospheric sciences, 42, 263–270, 1985.
- Högström, U.: Non-dimensional wind and temperature profiles in the atmospheric surface layer: A re-evaluation, in: Topics in Micrometeorology. A Festschrift for Arch Dyer, pp. 55–78, Springer, 1988.
- Högström, U., Hunt, J., and Smedman, A.-S.: Theory and measurements for turbulence spectra and variances in the atmospheric neutral  
595 surface layer, Boundary-Layer Meteorology, 103, 101–124, 2002.
- Hojstrup, J.: A statistical data screening procedure, Measurement Science and Technology, 4, 153, 1993.
- Holtslag, M. C., Bierbooms, W. A. A. M., and Van Bussel, G. J. W.: Wind turbine fatigue loads as a function of atmospheric conditions offshore, Wind Energy, 19, 1917–1932, 2016.
- Hristov, T., Friehe, C., and Miller, S.: Wave-coherent fields in air flow over ocean waves: Identification of cooperative behavior buried in  
600 turbulence, Physical review letters, 81, 5245, 1998.
- IEC 61400-1: IEC 61400-3 Wind Turbines Part 1: Design Requirements, 2005.

- Jacobsen, A. and Godvik, M.: Influence of wakes and atmospheric stability on the floater responses of the Hywind Scotland wind turbines, *Wind Energy*, 24, 149–161, 2021.
- Janssen, P. A.: Wave-induced stress and the drag of air flow over sea waves, *Journal of Physical Oceanography*, 19, 745–754, 1989.
- 605 Jiang, Q.: Influence of Swell on Marine Surface-Layer Structure, *Journal of the Atmospheric Sciences*, 77, 1865–1885, 2020.
- Jiang, Q., Wang, Q., Wang, S., and Gaberšek, S.: Turbulence adjustment and scaling in an offshore convective internal boundary layer: A CASPER case study, *Journal of the Atmospheric Sciences*, 77, 1661–1681, 2020.
- Johnson, H. K., Højstrup, J., Vested, H. J., and Larsen, S. E.: On the dependence of sea surface roughness on wind waves, *Journal of physical oceanography*, 28, 1702–1716, 1998.
- 610 Jonkman, J. and Musial, W.: Offshore code comparison collaboration (OC3) for IEA Wind Task 23 offshore wind technology and deployment, Tech. rep., National Renewable Energy Lab.(NREL), Golden, CO (United States), 2010.
- Kaimal, J. C. and Finnigan, J. J.: *Atmospheric Boundary Layer Flows: Their Structure and Measurement*, Oxford University Press, 1994.
- Kaimal, J. C., Wyngaard, J. C. J., Izumi, Y., and Coté, O. R.: Spectral characteristics of surface-layer turbulence, *Quarterly Journal of the Royal Meteorological Society*, 98, 563–589, 1972.
- 615 Kelly, M.: From standard wind measurements to spectral characterization: turbulence length scale and distribution, *Wind Energy Science*, 3, 533–543, 2018.
- Klipp, C.: Turbulent friction velocity calculated from the Reynolds stress tensor, *Journal of the Atmospheric Sciences*, 75, 1029–1043, 2018.
- Kolmogorov, A. N.: The local structure of turbulence in incompressible viscous fluid for very large Reynolds numbers, *Cr Acad. Sci. URSS*, 30, 301–305, 1941.
- 620 Kondo, J., Fujinawa, Y., and Naito, G.: Wave-induced wind fluctuation over the sea, *Journal of Fluid Mechanics*, 51, 751–771, 1972.
- Kristensen, L. and Jensen, N.: Lateral coherence in isotropic turbulence and in the natural wind, *Boundary-Layer Meteorology*, 17, 353–373, 1979.
- Kristensen, L., Panofsky, H. A., and Smith, S. D.: Lateral coherence of longitudinal wind components in strong winds, *Boundary-Layer Meteorology*, 21, 199–205, 1981.
- 625 Larsén, X. G., Petersen, E. L., and Larsen, S. E.: Variation of boundary-layer wind spectra with height, *Quarterly Journal of the Royal Meteorological Society*, 144, 2054–2066, 2018.
- Leys, C., Ley, C., Klein, O., Bernard, P., and Licata, L.: Detecting outliers: Do not use standard deviation around the mean, use absolute deviation around the median, *Journal of Experimental Social Psychology*, 49, 764–766, 2013.
- Longuet-Higgins, M. S.: On the statistical distribution of the heights of sea waves. J, *Journal of Marine Research*, 11, 245–266, 1952.
- 630 Lumley, J. and Panofsky, H.: *The Structure of Atmospheric Turbulence*, Interscience monographs and texts in physics and astronomy, Interscience Publishers, 1964.
- Mahrt, L., Vickers, D., Howell, J., Højstrup, J., Wilczak, J. M., Edson, J., and Hare, J.: Sea surface drag coefficients in the Risø Air Sea Experiment, *Journal of Geophysical Research: Oceans*, 101, 14 327–14 335, 1996.
- Mahrt, L., Vickers, D., Edson, J., Wilczak, J. M., Hare, J., and Højstrup, J.: Vertical structure of turbulence in offshore flow during RASEX, *Journal of Geophysical Research: Oceans*, 101, 14 327–14 335, 2001.
- 635 Mann, J.: The spatial structure of neutral atmospheric surface-layer turbulence, *Journal of fluid mechanics*, 273, 141–168, 1994.
- Mestayer, P.: Local isotropy and anisotropy in a high-Reynolds-number turbulent boundary layer, *Journal of Fluid Mechanics*, 125, 475–503, 1982.

- Mikkelsen, T., Larsen, S. E., Jørgensen, H. E., Astrup, P., and Larsén, X. G.: Scaling of turbulence spectra measured in strong shear flow near the Earth's surface, *Physica Scripta*, 92, 124 002, 2017.
- Monin, A. S.: The structure of atmospheric turbulence, *Theory of Probability & Its Applications*, 3, 266–296, 1958.
- Monin, A. S. and Obukhov, A. M.: Basic laws of turbulent mixing in the atmosphere near the ground, *Tr. Geofiz. Inst., Akad. Nauk SSSR*, 24, 163–187, 1954.
- Mouzakis, F., Morfiadakis, E., and Dellaportas, P.: Fatigue loading parameter identification of a wind turbine operating in complex terrain, *Journal of Wind Engineering and Industrial Aerodynamics*, 82, 69–88, 1999.
- Naito, G.: Spatial structure of surface wind over the ocean, *Journal of Wind Engineering and Industrial Aerodynamics*, 13, 67–76, 1983.
- Nielsen, F. G., Hanson, T. D., and Skaare, B.: Integrated dynamic analysis of floating offshore wind turbines, in: *International Conference on Offshore Mechanics and Arctic Engineering*, vol. 47462, pp. 671–679, 2006.
- Nybø, A., Nielsen, F. G., Reuder, J., Churchfield, M. J., and Godvik, M.: Evaluation of different wind fields for the investigation of the dynamic response of offshore wind turbines, *Wind Energy*, 23, 1810–1830, 2020.
- Peña, A. and Gryning, S.-E.: Charnock's roughness length model and non-dimensional wind profiles over the sea, *Boundary-layer meteorology*, 128, 191–203, 2008.
- Peña, A., Dellwik, E., and Mann, J.: A method to assess the accuracy of sonic anemometer measurements, *Atmospheric Measurement Techniques*, 12, 237–252, 2019.
- Power Technology: Full circle: decommissioning the first ever offshore windfarm, <https://www.power-technology.com/features/full-circle-decommissioning-first-ever-offshore-windfarm/>, [Online; accessed 28-March-2021], 2020.
- Putri, R., Obhrai, C., Jakobsen, J., and Ong, M.: Numerical Analysis of the Effect of Offshore Turbulent Wind Inflow on the Response of a Spar Wind Turbine, *Energies*, 13, 2506, 2020.
- Robertson, A., Jonkman, J., Vorpahl, F., Popko, W., Qvist, J., Frøyd, L., Chen, X., Azcona, J., Uzunoglu, E., Guedes Soares, C., et al.: Offshore code comparison collaboration continuation within IEA wind task 30: phase II results regarding a floating semisubmersible wind system, in: *International Conference on Offshore Mechanics and Arctic Engineering*, vol. 45547, p. V09BT09A012, American Society of Mechanical Engineers, 2014.
- Robertson, A. N., Shaler, K., Sethuraman, L., and Jonkman, J.: Sensitivity analysis of the effect of wind characteristics and turbine properties on wind turbine loads, *Wind Energy Science*, 4, 479–513, 2019.
- Rosner, B.: Percentage points for a generalized ESD many-outlier procedure, *Technometrics*, 25, 165–172, 1983.
- Sacré, C. and Delaunay, D.: Structure spatiale de la turbulence au cours de vents forts sur différents sites, *Journal of Wind Engineering and Industrial Aerodynamics*, 41, 295–303, 1992.
- Sanchez Gomez, M. and Lundquist, J. K.: The effect of wind direction shear on turbine performance in a wind farm in central Iowa, *Wind Energy Science*, 5, 125–139, 2020.
- Saranyasoonorn, K., Manuel, L., and Veers, P. S.: A comparison of standard coherence models for inflow turbulence with estimates from field measurements, *J. Sol. Energy Eng.*, 126, 1069–1082, 2004.
- Sathe, A. and Bierbooms, W.: Influence of different wind profiles due to varying atmospheric stability on the fatigue life of wind turbines, *Journal of Physics: Conference Series*, 75, 012 056, 2007.
- Sathe, A., Mann, J., Barlas, T., Bierbooms, W., and van Bussel, G.: Influence of atmospheric stability on wind turbine loads, *Wind Energy*, 16, 1013–1032, 2013.



- Schotanus, P., Nieuwstadt, F., and De Bruin, H.: Temperature measurement with a sonic anemometer and its application to heat and moisture fluxes, *Boundary-Layer Meteorology*, 26, 81–93, 1983.
- Sempreviva, A. M. and Gryning, S. E.: Humidity fluctuations in the marine boundary layer measured at a coastal site with an infrared humidity sensor, *Boundary-layer meteorology*, 77, 331–352, 1996.
- 680 Sheinman, Y. and Rosen, A.: A dynamic model of the influence of turbulence on the power output of a wind turbine, *Journal of Wind Engineering and Industrial Aerodynamics*, 39, 329–341, 1992.
- Sjöblom, A. and Smedman, A.-S.: Vertical structure in the marine atmospheric boundary layer and its implication for the inertial dissipation method, *Boundary-layer meteorology*, 109, 1–25, 2003a.
- Sjöblom, A. and Smedman, A.-S.: Vertical structure in the marine atmospheric boundary layer and its implication for the inertial dissipation method, *Boundary-layer meteorology*, 109, 1–25, 2003b.
- 685 Smedman, A. S., Högström, U., and Sjöblom, A.: A note on velocity spectra in the marine boundary layer, *Boundary-layer meteorology*, 109, 27–48, 2003.
- Smedman-Högström, A.-S. and Högström, U.: Spectral gap in surface-layer measurements, *Journal of Atmospheric Sciences*, 32, 340–350, 1975.
- 690 Soucy, R., Woodward, R., and Panofsky, H.: Vertical cross-spectra of horizontal velocity components at the Boulder observatory, *Boundary-Layer Meteorology*, 24, 57–66, 1982.
- Stiperski, I. and Rotach, M. W.: On the measurement of turbulence over complex mountainous terrain, *Boundary-Layer Meteorology*, 159, 97–121, 2016.
- Stull, R. B.: *An Introduction to Boundary Layer Meteorology*, Kluwer Academic Publishers, 1 edn., 1988.
- 695 Tamura, H., Drennan, W. M., Collins, C. O., and Graber, H. C.: Turbulent airflow and wave-induced stress over the ocean, *Boundary-Layer Meteorology*, 169, 47–66, 2018.
- Taylor, G. I.: The spectrum of turbulence, *Proceedings of the Royal Society of London. Series A-Mathematical and Physical Sciences*, 164, 476–490, 1938.
- Tuomi, L. and Huess, V.: Product user manual for Baltic Sea wave analysis and Forecasting Product, Tech. Rep. CMEMS-BAL-PUM-003-010, Finnish Meteorological Institute, finland, 2020.
- 700 Van der Hoven, I.: Power spectrum of horizontal wind speed in the frequency range from 0.0007 to 900 cycles per hour, *Journal of Atmospheric Sciences*, 14, 160–164, 1957.
- Veers, P., Dykes, K., Lantz, E., Barth, S., Bottasso, C. L., Carlson, O., Clifton, A., Green, J., Green, P., Holttinen, H., et al.: Grand challenges in the science of wind energy, *Science*, 366, 2019.
- 705 Vickers, D. and Mahrt, L.: Quality control and flux sampling problems for tower and aircraft data, *Journal of atmospheric and oceanic technology*, 14, 512–526, 1997.
- Vickers, D. and Mahrt, L.: The cospectral gap and turbulent flux calculations, *Journal of atmospheric and oceanic technology*, 20, 660–672, 2003.
- Weber, R. O.: Remarks on the definition and estimation of friction velocity, *Boundary-Layer Meteorology*, 93, 197–209, 1999.
- 710 Weiler, H. S. and Burling, R.: Direct measurements of stress and spectra of turbulence in the boundary layer over the sea, *Journal of Atmospheric Sciences*, 24, 653–664, 1967.
- Welch, P.: The use of fast Fourier transform for the estimation of power spectra: a method based on time averaging over short, modified periodograms, *IEEE Transactions on audio and electroacoustics*, 15, 70–73, 1967.

- Wendell, L., Gower, G., Morris, V., and Tomich, S.: Wind turbulence characterization for wind energy development, Tech. rep., Pacific Northwest Lab., Richland, WA (United States), 1991.
- Wilczak, J., Oncley, S., and Stage, S.: Sonic anemometer tilt correction algorithms, *Boundary-Layer Meteorology*, 99, 127–150, 2001.
- WMO: Guide to meteorological instruments and methods of observation, Secretariat of the World Meteorological Organization, 1983.
- Wyngaard, J. and Coté, O.: Cospectral similarity in the atmospheric surface layer, *Quarterly Journal of the Royal Meteorological Society*, 98, 590–603, 1972.
- 715 Wyngaard, J. C.: On the surface-layer turbulence, In D. A. Haugen, Ed., *Workshop on Micrometeorology*, American Meteorological Society, pp. 101–149, 1973.
- 720 Wyngaard, J. C. and Coté, O. R.: The budgets of turbulent kinetic energy and temperature variance in the atmospheric surface layer, *Journal of Atmospheric Sciences*, 28, 190–201, 1971.